Understanding wave energy converters dynamics: High-fidelity modeling and validation of a moored floating body

(Article begins on next page)
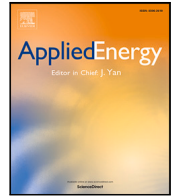
Understanding wave energy converters dynamics: High-fidelity modeling and validation of a moored floating body

Oronzo Dell'Edera [*], Francesco Niosi, Pietro Casalone, Mauro Bonfanti, Bruno Paduano, Giuliana Mattiazzo

Marine Offshore Renewable Energy Lab (MOREnergy Lab), Department of Mechanical and Aerospace Engineering, Politecnico di Torino, Via Duca Degli Abbruzzi, 24, Turin, 10129, Italy

ARTICLE INFO

ABSTRACT

In ocean engineering, one of the most challenging phenomena to replicate is the interaction between waves and a moored floating body. Accurately evaluating such systems is essential for minimizing uncertainties, mitigating risks, and advancing technologies like wave energy converters. For this purpose, this study aims to develop a high-fidelity numerical model capable of reducing reliance on costly experimental campaigns during the device design phases. The model integrates a fluid dynamics module based on the Navier–Stokes equations, implemented in Star CCm+, with a mooring model utilizing a mass–spring–damper system, specifically MoorDyn. The primary objective is to introduce this coupled approach and demonstrate its efficacy through validation against experimental data from two distinct wave energy converters: ISWEC and PeWEC. The validation process encompasses comprehensive comparisons between simulated and observed kinematic behavior, mooring tensions, and crucially, pressure loads. Results indicate that the model is able to faithfully predict the complex phenomena involving a moored floating body, affirming the accuracy and reliability of the proposed coupling methodology. The coupling developed is available online link, where a simplified case study is present to show how to compile the library and add it in the numerical model.

1. Introduction

Marine energy stands as one of the most promising renewable resources on our planet [1,2], with the potential to generate between 20,000 and 80,000 TWh per year, exceeding global power consumption [3,4]. Among the technologies harnessed for this purpose, wave energy converters (WECs) emerge as promising technologies, as their estimated potential in Europe alone is around 2800 TWh annually [5]. Unfortunately, WECs development has historically been slower compared to other renewable energy due to considerable obstacles emerging from the complex design that has to face with the hostile marine environment. In the initial design phases, linear models based on potential flow are widely employed for their computational efficiency, facilitating the exploration of numerous configurations [6]. However, the subsequent verification process necessitates more advanced tools, such as computational fluid dynamics (CFD) [7] which, despite their computational demands, offer unparalleled accuracy by incorporating viscous, turbulent, and nonlinear phenomena, demanding fewer assumptions [8,9]. Additionally, CFD models can provide accurate representation of pressure loads, which play a crucial role in the

verification process, essential for validating the structural design and evaluating the safe life of the device [10].

Mid-fidelity models have shown promise for the rapid and accurate evaluation of floating body responses, including nonlinear effects [11]. However, they still require calibration using CFD models or experimental data. For instance, [12] demonstrates how low-fidelity models can be enhanced by incorporating viscous damping from CFD. Though the application of low/mid-fidelity models, can yield satisfactory results when describing small wave conditions and corresponding motion responses [13], for resonant devices like wave energy systems, the use of high-fidelity models is essential to adequately represent significant nonlinear phenomena such as wave-in-deck interactions, turbulent forces, and slamming forces.

The hydrodynamics of a floating body can be accurately modeled using CFD software. Nonetheless, for a comprehensive analysis of overall dynamics, it is imperative to consider all significant influences, including moorings. Moorings address the critical station-keeping challenge, which is vital for the positional maintenance of WECs. Mooring design is a complex and critical aspect that must adhere to international standards (*e.g.,* [14,15]), which mandate a thorough analysis

of mooring systems against extreme and operational environmental conditions [16]. While most international standards focus on mooring design for offshore applications, with the notable exception of IEC standards, the station-keeping problem for wave energy systems is specifically addressed in [17,18]. Additionally, a mooring system must not only ensure the system survivability under any environmental condition but also avoid negatively impacting the dynamics of the system or, more specifically, the WEC energy harvesting capability. The impact of the mooring system on the dynamics of WECs, analyzed through a linear data-based model, has been explored in literature such as [19,20], which delve into the response of generic floating bodies and the consequent energy harvest using a frequency-domain approach. The inclusion of nonlinearities in the performance evaluation of moored wave energy systems is discussed in [21,22], focusing on devices exhibiting pitching motion. Additionally, Gubesch et al. [23] investigate the experimental response of an oscillating water column system under fixed conditions, moored with both taut and catenary systems, and report a significant decrease in device performance. The role of mooring systems under both operational and extreme environmental conditions is further discussed in [24–26]. Moreover, moorings may demonstrate markedly nonlinear behavior, making their comprehensive integration into a manageable floater model challenging [27]. While the impact of moorings on device dynamics is well-documented in existing literature, most contemporary research in wave energy primarily focuses on mooring system design [28–30].

A straightforward, simplified, solution to model the mooring system in CFD software is incorporating a quasi-static mooring model for a floating object, as demonstrated in [31,32] and in [33,34] in which Star CCm+ and OpenFOAM are used, respectively. While this approach may be sufficient for an initial analysis, it proves inadequate for accurately modeling a floating body, as it tends to heavily underestimate mooring loads [35] and, the associated floater dynamics. Additionally, OpenFOAM has been coupled with MoorDyn [36,37] and Moody [38], validating these models against experimental data. While device response results to be faithfully described in heave and surge motions, the pitch motion was consistently underestimated by these models. This problem can be attributed to the use of the deforming mesh model, which follows body motion. Models based on this assumptions, can be representative if the rotation of the body is small, as demonstrated in [39,40] however, for a WEC, particularly one based on pitch, the use of the deforming mesh directly introduce numerical damping for high rotations as the quality of the mesh decrease rapidly [41,42], leading the simulation to heavily underestimate the pitch dynamics and, consequently, the tension in the mooring system.

It is worth noting that, though most applications propose the use of the deforming mesh, in OpenFOAM, an overset approach can be also used [43,44]. Nevertheless, the overset method has some drawbacks, such as higher computational costs, which according to [45] can double the simulations run time, and difficulties in creating a good interface between the two regions [46]. Finally, among high fidelity models, another increasingly popular software able to perform high fidelity simulation is DualSPHysics, based on the smooth particle hydrodynamics (SPH) theory, a mesh-free approach, which has been extensively validated against experimental data [47,48]. While SPH models have shown good overall performance in the simulation of free surface flow [49,50], they often struggle to accurately represent small amplitude motions. In the case of offshore wind turbine platforms, which experience significantly smaller motions compared to WECs, SPH models tend to underestimate both pitch and surge [51]. This discrepancy arises from the introduction of artificial damping by the numerical model, particularly when the motion of the floating body is relatively small compared to the particle size [52].

Recent developments have focused on hybrid Eulerian–Lagrangian methods, which combine the strengths of both approaches. For example, the Particle-In-Cell (PIC) model [53] integrates the advantages of mesh-based and particle-based methods. These hybrid models have

shown promise in accurately simulating WECs, as demonstrated in blind tests published by [54], which highlighted their effectiveness in focused wave interactions with floating structures. While this methodology has shown potential, there are still some issues to resolve as it is relatively new. Notably, the memory storage requirements for the PIC model are demanding due to the double grid system. Additionally, the PIC model may predict inaccurate damping effects as demonstrated in the comparisons presented by [54], where the pitch predicted by the PIC model was overestimated relative to the experimental results.

To synthesize, high-fidelity simulations represent in general a useful tool for validation of low-fidelity numerical models. Nevertheless, for wave energy resonant devices, the use of high-fidelity models can be significantly important in both, validation and direct design phase [55], since a representative pressure field can be evaluated only by leveraging such nonlinear models. Accordingly, this study aims to:

- Propose a high-fidelity simulation tool: though the wave energy case is analyzed, this study aims to delve into the definition of a representative high-fidelity simulation tool for floating objects, by coupling a dynamic mooring model with a CFD solver. This coupling is also generalized and uploaded for external users.
- Validating the system response against experimental data: to achieve this point, the data of two experimental campaigns have been adopted to test the tool faithfulness with representative conditions which involve as much nonlinear actions.
- Analyze the pressure field on the hulls: to acquire data on the pressure field, in both experimental campaigns several pressure gauges have been used, and the data are compared to the numerical model to assess the model performance in describing the pressure field, which can be essential in design phase.

Among the available solvers for hydrodynamics and mooring computation, Star CCm+ and MoorDyn are herein proposed. In contrast the other CFD solvers, Star CCm+ offer a comprehensive framework for simulating fluid–structure interactions, with the dynamic fluid body interaction module (DFBI), which consent the creation of two separate region, one following the body and one static external region representing the numerical wave tank. This representation allow a more faithful representation and reduce numerical errors. Nevertheless, the representation of mooring systems in Star CCm+ has its limitations. The catenary model provides a simple and efficient way to model catenaries, offering flexibility in specifying mass per unit length, tension, and initial shape. However, this model has limitations, including the absence of buoyancy correction, neglect of fluid forces acting on the catenary, and the potential for catenaries to pass through bodies or boundaries in certain circumstances. Although the introduction of discrete element method (DEM) in version 2302 addresses some of these issues, it comes with its drawbacks, such as incompatibility with the adaptive mesh refinement (AMR) and increased computational expense, particularly for high-tension cables [56]. On the other hand, MoorDyn was specifically designed for predicting the dynamics of typical mooring systems [57]. It supports arbitrary line interconnections, clump weights, floats, and different line properties. The model accounts for axial stiffness and damping forces, weight and buoyancy forces, hydrodynamic forces from Morison's equation, and vertical spring–damper forces from contact with the seabed.

The case studies adopted for the model validation regard the ISWEC and PeWEC devices. In both cases, the wave energy systems are pitching resonant devices, representing interesting and representative case studies due to the high variation of the waterline and the wave-in-deck effects, which result in significant nonlinear forces. Furthermore, the devices feature both a semi-taut and a catenary mooring, ensuring the analysis and testing of the coupling in different scenarios, with the restoring force of the catenary weight-based and the semi-taut one stiffness-based.

The remaining of this study, is organized as follows: in Section 2 the numerical models, by including the coupling of the CFD-mooring solver

coupling, are discussed. In Section 3, the ISWEC and PeWEC case studies are introduced and described, in Section 4, the experimental data are compared to the numerical one aiming to validate the high-fidelity tool and, finally, in Section 5 the conclusions are outlined.

2. Numerical modeling

The effective simulation of WECs demands a comprehensive numerical approach that accurately captures the complex interplay between fluid and floater dynamics. In this section, we present the numerical models employed in this study, encompassing the CFD model setup, mooring model descriptions, and the coupling methodology.

2.1. Fluid dynamics model

The software used for the CFD model is Star CCm+, specifically version 2022.1. In this software, the motion of an incompressible fluid is described analytically in a deterministic way by the Navier–Stokes equations:

$$\nabla \cdot v = 0, \tag{1}$$

$$\frac{\partial v}{\partial t} + \nabla \cdot (vv) = -\frac{1}{\rho}\nabla p + g + \frac{1}{\rho}\nabla \cdot \bar{\tau}, \tag{2}$$

where, $\rho \in \mathbb{R}^+$ represents the water density, $\{v, p, g, \tilde{\tau}\} : \mathbb{R}^+ \rightarrow \mathbb{R}^3, t \mapsto \{v(t), p(t), g(t), \tilde{\tau}(t)\}$ are the fluid velocity, the pressure field, the gravitational field, and the shear stress tensor, respectively. For an incompressible fluid, the shear stress tensor is defined as:

$$\tau_{ij} = \mu\left(\frac{\partial v_i}{\partial x_j} + \frac{\partial v_j}{\partial x_i}\right), \tag{3}$$

where $\mu \in \mathbb{R}^+$ is the dynamic viscosity of the fluid. These equations cannot be solved in closed form but can be solved numerically by discretizing the domain into finite volumes. Additionally, it is important to note that the Reynolds number associated with these simulations makes the direct Navier–Stokes equations infeasible, and an approximation must be made. In this specific case, Reynolds averaged Navier–Stokes equations (RANS) are employed to average the flow properties over time. To properly represent the turbulence problem, the $k - \varepsilon$ model is adopted, where $k : \mathbb{R}^+ \rightarrow \mathbb{R}^+, t \mapsto k(t)$ is the turbulent kinetic energy and $\varepsilon : \mathbb{R}^+ \rightarrow \mathbb{R}^+, t \mapsto \varepsilon(t)$ is the dissipation rate [58]. The turbulence model is coupled with a wall function for treating high-gradient regions near walls [59].

While the fluid is well described by the over mentioned models, the waterline represents the interface of two different fluids, which needs to be modeled in detail in order to represent the wave dynamics accurately. This requirement leads us to the application of the volume of fluid (VOF) model [60,61], which defines the different fluid phases using the scalar function:

$$\alpha_2 = 1 - \alpha_1, \tag{4}$$

$$\rho = \alpha_1\rho_1 + \alpha_2\rho_2 = (\rho_1 - \rho_2)\alpha_1 + \rho_2, \tag{5}$$

where $\alpha_i \in [0, 1]$ is the volume fraction of phase i and ρ_i is the density of phase i. In the software, the interface between the two fluids, called the free surface, is defined at the point where the value of α_1 (or α_2) is locally equal to 0.5 (Fig. 1). To achieve a precise description of the interface between these phases, we employ the High-Resolution Interface Capturing (HRIC) scheme. The HRIC scheme is designed to accurately track the sharp interfaces between immiscible fluids, such as air and water, thus allowing for an accurate representation of the wave interaction with the WEC [62].

Unfortunately, the coupling of the turbulence model with the VOF model is intrinsically unstable, leading to an exponential growth in turbulent viscosity [63]. This phenomenon hinders correct wave transport, causing excessive damping of the wave over a long time series. Though

the proposed tool is tested in the Star CCm+ version 2022.1, it is worth mentioning that the viscosity stability problem is currently fixed in the version 2310, implementing the methodology discussed in [63]. For this reason, to prevent a non-physical grow of turbulence viscosity, the methodology presented by Casalone et al. [64] has been implemented, which limit the maximum turbulent viscosity in the domain.

To reduce potential sources of error, the numerical wave tank has been calibrated in a semi-2D environment to reproduce the target wave height. The semi-2D environment refers to a 3D domain with only a single cell in the Y direction, as the VOF model is not supported in combination with 2D physics by Star CCm+. Furthermore, it is worth nothing that the wave is generated by leveraging an input/output frequency response which depends on the wave steepness, the numerical discretization and the Courant–Friedrichs–Lewy number (CLF). The frequency response is obtained via an iterative process, as described in [56]:

$$\alpha_{in}^{i+1} = \alpha_{in}^i \frac{\alpha_{trg}}{\alpha_{out}^i} \tag{6}$$

where α_{in}^i is the input amplitude to the numerical model at iteration i, α_{out}^i is the output amplitude of the numerical model and α_{trg} is the target amplitude. For regular waves this process converge after 2 iteration. As the input/output frequency response strongly depends on the numerical setup, it is recommended to perform calibration for each wave to be tested, as it is possible to try to reduce potential sources of numerical error yet not eliminate them completely.

For detailed information about the numerical model mesh and boundary condition, the reader can refer to the technical note in Appendix.

2.2. Mooring model

This section examines the primary characteristics of the mooring solver utilized in this investigation. In the context of wave energy systems, the mooring system is effectively modeled using a dynamic solver, with particular emphasis on the dynamic finite-difference solver [65]. In this approach, the mooring problem is addressed through a lumped-mass approach (refer to Fig. 2).

In a lumped-mass approach, the dynamics equation for the mooring line, considering the kth node, can be formulated as follows:

$$(m_k + a_k)\ddot{r}_k = f_{EA,k-} + f_{EA,k+} + f_{C,k-} + f_{C,k+} + f_{B,k} + f_{Dn,k} + f_{Da,k} + f_{ext,k}. \tag{7}$$

In this formulation, $m_k, a_k \subset \mathbb{R}^{3\times3}$ denotes the mass and the added mass of the kth node, respectively. $r_k : \mathbb{R}^+ \rightarrow \mathbb{R}^3, t \mapsto r_k(t)$ represents the position of the kth node relative to a global fixed frame of reference $Ox_1x_2x_3$ located on the waterline. $f_{EA}, f_C : \mathbb{R}^+ \rightarrow \mathbb{R}^3, t \mapsto f_{EA}, f_C(t)$ are the axial stiffness and damping forces, respectively, due to the line section properties. Note that the subscripts $k+, k-$ express the forces caused by the interaction between nodes k and $k + 1$, and k and $k - 1$, respectively. The node net buoyancy force is denoted by $f_{B,k}(t) \in \mathbb{R}^3$, and $f_{Dn,k}, f_{Da,k} : \mathbb{R}^+ \rightarrow \mathbb{R}^3, t \mapsto f_{Dn,k}(t), f_{Da,k}(t)$ represent the drag normal and axial forces, respectively, caused by the velocity of the kth node in the fluid. Finally, $f_{ext,k} : \mathbb{R}^+ \rightarrow \mathbb{R}^3, t \mapsto f_{ext,k}$ represents external actions, such as the interaction of the node with the seabed, or forces applied on the node by line attachments (e.g., buoy or clump-weights), among others. The specific solver utilized in this study is MoorDyn [66], a freely available software developed and validated by Matthew Hall [57]. Please note that, though the study presented herein is based on the previous MoorDyn version (*i.e.* v1), the current version [67] expands the modeling capabilities implementing, among others, cable bending stiffness [68].
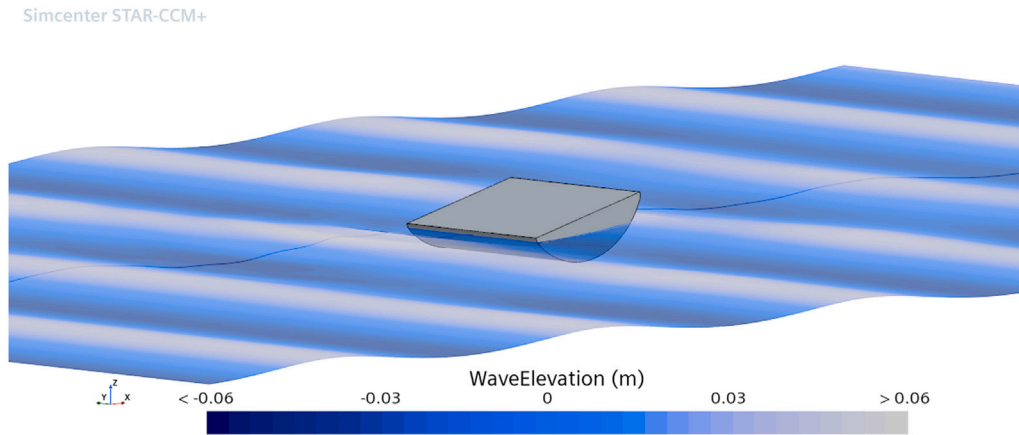
Simcenter STAR-CCM+

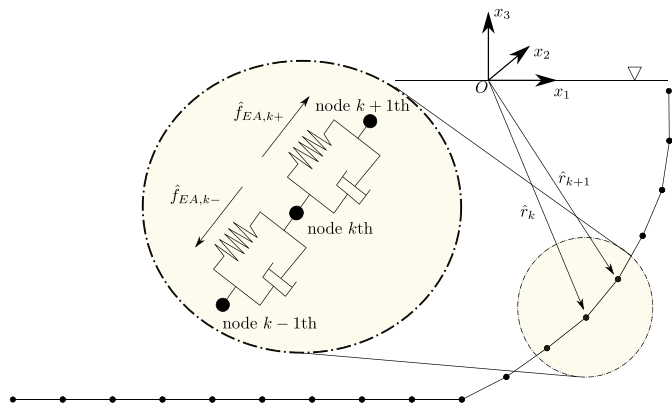**Fig. 1.** Free surface during a simulation. The mooring system is not visible in the simulation.

Fig. 2. Mooring solver modeling scheme. Each line between the defined nodes is modeled with a lumped-mass system.
Source: Adapted from [55]

Table 1
Input parameters required before compiling the library uclib.cpp.

Λ	If the simulation involves the entire device and there is no symmetry involved, the scale factor Λ should be set to 1. However, if the simulation exploits symmetry along the y-axis (e.g., $y = 0$ symmetry), the Λ factor should be set to 2.
t_{in}	Inner iteration of Star CCm+. The value needs to be coherent with the simulations.
x_{CoG}, y_{CoG}, z_{CoG}	Coordinate of the CoG of the body in the Laboratory Coordinate system.
Φ, Θ, Ψ	Initial rotation of the body coordinate system in respect to its rest condition. Useful in Free-Decay tests.

2.3. Coupling

Within this Section the coupling method of both mathematical models, presented in Sections 2.1 and 2.2, respectively, is discussed. The general workflow of the coupling is reported in Fig. 3. Star CCm+ serves as the simulation master, dictating the invocation of the library that contains MoorDyn. During each inner iteration, hydrodynamic loads are computed and relayed to the DFBI. Subsequently, the DFBI adds these loads with mooring forces and moments calculated at the end of the previous time step, and proceed to evaluate the body kinematics. The resulting translation and rotation of the center of gravity (CoG) are then fed back to MoorDyn, which computes mooring forces and momentum for the next iteration. For the initial time step, mooring forces and moments are initialized from the static equilibrium performed prior to the beginning of the simulation.

To generate the library, compile the provided makefile using the command "make makefile comp" in a Linux operating system. It is important that, the MoorDyn-master folder, containing MoorDyn (already compiled in the subfolder "CompileSO"), and the coupling folder with the uclib.cpp file are available. In details, the uclib.cpp file acts as an interface, interacting with MoorDyn, invoking functions, and acquiring variables from Star CCm+. It defines two fundamental functions, "MooringForces" and "MooringMoments" (responsible of providing to the master software the mooring forces and moments, respectively), which Star CCm+ calls at the end of each iteration to evaluate mooring loads through MoorDyn native functions. These functions update only at the end of each time step despite being called during each inner

iteration. The main parameters defining the coupling aspects in the uclib.cpp file are outlined in Table 1.

After generating the library, the resulting .so file can be loaded into Star CCm+. The characteristics of the mooring system need to be stored in a lines.txt file inside the "Mooring" folder; an example is also included in GitHub repository. An annexed java macro for Star CCm+ facilitates the automatic setup of the coupling. The macro loads the previously created library into Star CCm+, assigning it to the DFBI user-defined coupling for the body "body 1". The "User Code" option is selected for both forces and moments in the user-defined coupling of the DFBI. The respective "MooringForces" and "MooringMoment" functions are chosen for forces and moments during the coupling setup. It is worth mentioning that in the lines.txt files, the connection to the vessel must be set considering the CoG coordinate system. Additionally, the coupling requires two custom field functions in Star CCm+, containing the distance of the CoG from the origin of the laboratory coordinate system and the rotation of the body. The other functions called in the library are native functions of Star CCm+.

3. Case study

Before delving into the validation of the proposed tool against experimental data, this section discusses the two case studies proposed as representative benchmarks and highlights the motivations that drove the choice of such case studies. While mooring systems are designed to address the station-keeping problem, ensuring the device serviceability, these should ideally have minimal impact on device dynamics, especially under operational conditions [21,22]. This problem is evidently non-trivial. Moreover, it is indeed true that if the mooring significantly influences the device dynamics, the associated response, including the definition of the pressure field, needs to be determined by integrating such relevant actions. It is indeed acknowledged in the current
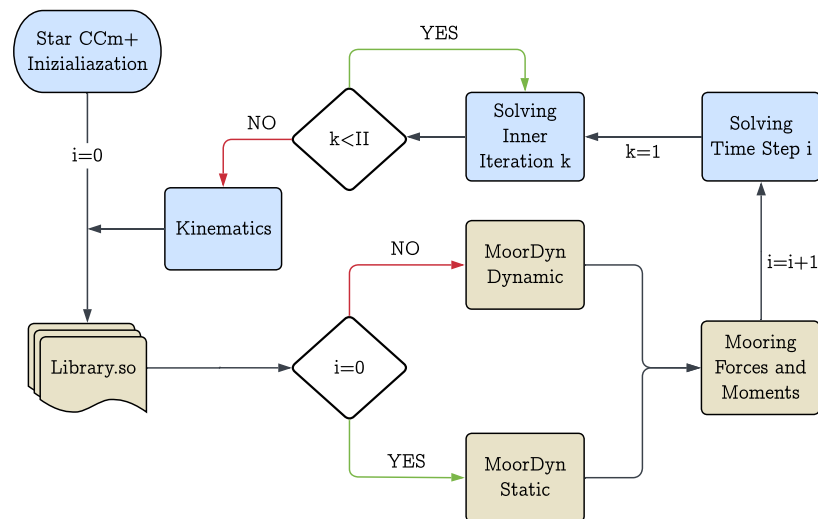
Fig. 3. Numerical coupling between Star CCm+ and MoorDyn: schematic representation of the simulation library (Library.so) call for the evaluation of the moorings forces and moments. The iteration continues until the simulation time reaches the target time.

literature panorama that, although the mooring system can affect the dynamics of any wave energy converting system [26,69,70], one of the most affected degrees-of-freedom is the pitch [20]. Accordingly, to fully understand the potential, importance, and limitations of the proposed design tool, it has been validated with two different pitching wave energy systems: the pendulum wave energy converter (PeWEC) and the inertial sea wave energy converter (ISWEC).

The PeWEC is the result of a collaboration between MORELab and ENEA, and as of today, it is a technology at TRL 5. PeWEC is capable of extracting energy from the wave motion by harnessing the oscillation of the pendulum inserted inside the hull [71].

The ISWEC represents the major counterpart of PeWEC, as it has a higher TRL, specifically 7. The ISWEC is the outcome of a collaboration between MORELab and Eni spa. Its working principle is based on the motion of a Power Take-Off (PTO) axis excited by the combined action of a gyroscopic unit and the device pitch motion [72].

Both devices utilize electro-mechanical systems sealed inside a monolithic, prismatic hull to protect these systems from the harsh marine environment. However, in the current study, the electricity output is not present. For ISWEC tests were performed without the Power Take-Off (PTO) system enabled, resulting in no electricity output. Similarly, for the PeWEC, the energy harvesting system was not present during this particular experimental campaign.

The decision to use two different but similar devices for validating the proposed tool is based on the differences in the corresponding mooring systems. As moorings are a crucial part of this study, the current validation covers both a generic semi-taut mooring system and a catenary-based mooring, where the restoring force is generated by the stiffness of the line and the linear weight, respectively. For a comprehensive description, readers are referred to Sections 3.2 and 3.3.

3.1. Experimental setup

The towing tank used for the experiments is 135 m long, 9 m wide, and 4.2 m deep, equipped with a wave maker capable of generating regular and irregular waves within a period range of 0.8 to 4 s and wave amplitude range of 0.08 to 0.20 m. The wave maker generates the waves adopting 1st order linear theory. An artificial seabed has been constructed from fiberglass panels and positioned at a depth of 1.28 m in the tank, which is the water depth of the experiments. The ISWEC and PeWEC models were placed 65 m from the wave maker, at the center of the wave tank. The experimental wave elevation measurements related to empty tank tests are considered in the same

position of the devices. A representation of the experimental facilities is reported in Fig. 4.

Two acquisition systems were employed to measure the 6 DOF device motions: the Qualisys® optical motion tracking system and an onboard IMU (Inertial Motion Unit) system. The optical motion tracking system involved three cameras placed on the carriage back, facing the device, and five Qualisys markers on the deck to accurately capture rotational and translational motions. The onboard system consisted of a National Instruments® compact RIO (cRIO) controller with analog and digital I/O modules, powered by batteries and equipped with a Wi-Fi router for real-time data transmission. The cRIO controller, programmed in the LabVIEW® environment, acquired data from an Xsens MTI-30 IMU, four load cells, and 27 pressure sensors at a frequency of 20 Hz. Synchronization between the two acquisition systems was achieved through a digital trigger signal from the cRIO controller. Calibration was conducted to convert the electrical signals from load cells and pressure sensors into physical units. For sake of clarity, in Fig. 5 is reported a block scheme of the acquisition system. In both devices, the load cells (LC) are positioned at the fairleads of each mooring line. During regular wave tests, the Power Take-Off system of the WECs is disconnected, thus no electricity output is acquired.

3.2. The ISWEC case

The ISWEC experimental campaign took place in Naples, Italy, in 2021. The mooring system employed is a spread hybrid, semi-taut mooring system consisting of a symmetrical pattern of 4 mooring lines (refer to Fig. 6).

Each mooring line comprises a catenary and a polyester section. The catenary section serves to prevent the line from clashing with the seabed (by leveraging the buoyancy force of a subsurface jumper) and to keep the polyester section out of the splash zone (air–water interface) [14]. The properties of the polyester have been determined through experimental tests [73]. The ISWEC hull is equipped with four rows of pressure gauges to characterize the pressure field across the entire device (see Fig. 12). Device kinematics were captured using an in-board MTi and an optical Qualisys motion tracking unit. For a comprehensive description of the experimental campaign and associated tests, please refer to [55].

3.3. The PeWEC case

The PeWEC experimental campaign, conducted in Naples, Italy, in 2021, utilized a spread catenary mooring system. This system features

Fig. 4. On the left, the dynamometric carriage from which the acquisitions are made, with PeWEC in the water. The yellow circles indicate the cameras of the Qualisys system. On the right, an image of the artificial seabed.
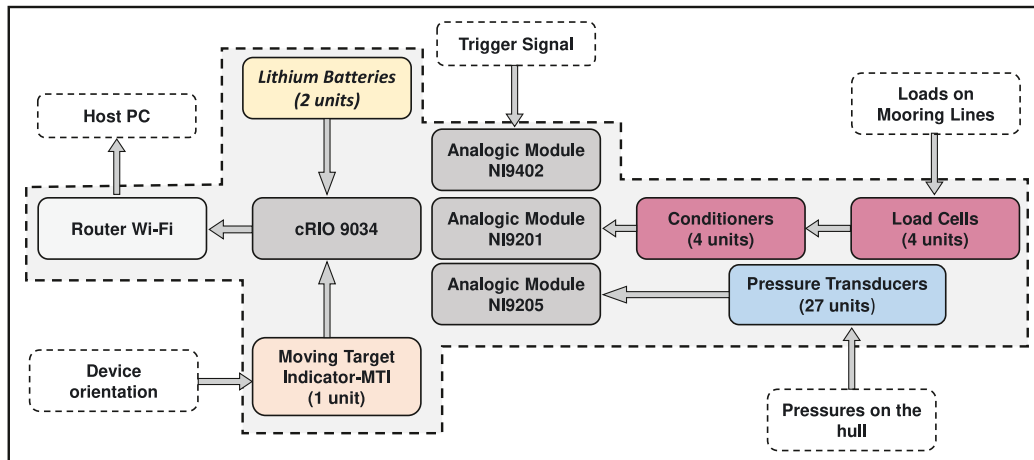

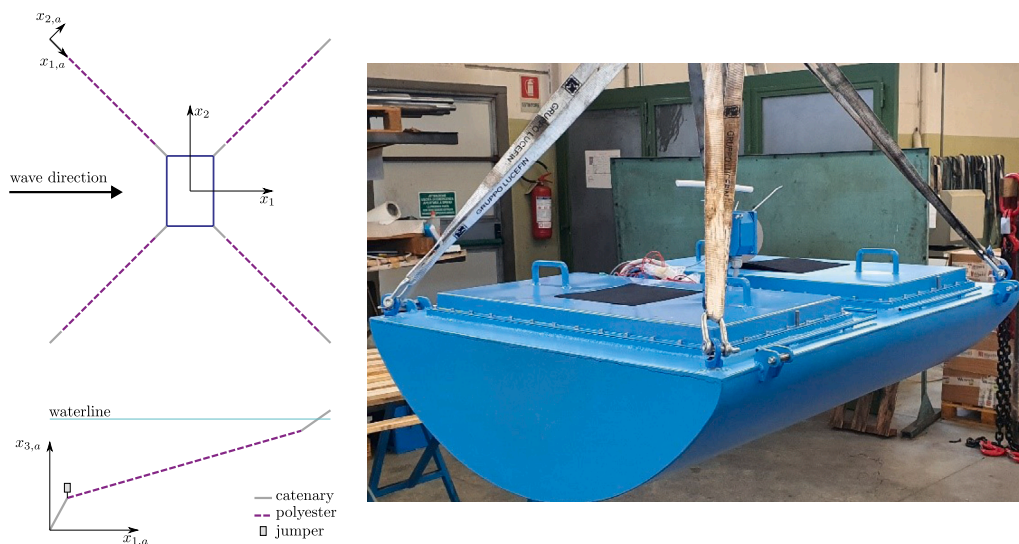**Fig. 5.** Block scheme of the acquisition system.

Fig. 6. Top left: spread mooring configuration of the ISWEC. Bottom left: Mooring line section and attachment details. Right: the ISWEC prototype.
Source: Adapted from [10]

a symmetrical arrangement of four mooring lines, as depicted in Fig. 7. Each mooring line is composed of a catenary, nine clump weights, and a jumper, with detailed parameters provided in [74]. The clump weights serve to increase the restoring force of the laid mooring line, as this line section exerts a predominant influence on the device survivability

in harsh conditions, while the jumper plays a crucial role in supporting the catenary's weight, allowing the WEC freedom in movements [22].

The PeWEC hull is equipped with four rows of pressure gauges, strategically positioned to characterize the pressure field across the entire device (see Fig. 17). As for the experimental tests conducted
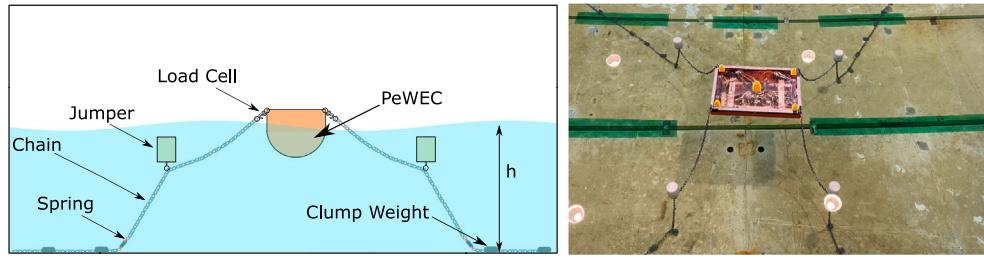
Fig. 7. On the left, the sketch of PeWEC mooring system. Adapted from [75]. On the right, the PeWEC prototype during the experimental campaign.

Table 2
Model-Scale characteristics of the PeWEC hull.

Parameter	SI Unit	Exp. value
Mass (M)	(kg)	72.360
Draft (T)	(m)	0.192
Vertical Position of CoG from deck (V_{CG})	(m)	−0.139
Roll Moment of Inertia (I_{44})	(kg m^2)	5.827
Pitch Moment of Inertia (I_{55})	(kg m^2)	3.334
Yaw Moment of Inertia (I_{66})	(kg m^2)	7.388

Table 3
Model-Scale characteristics of the PeWEC mooring system.

Description	Model-scale	SI Unit
Chain Description		
Mass per unit length	0.651	(kg/m)
Outer diameter	0.0057	(m)
Jumper Description		
Mass	0.512	(kg)
Volume	0.0016	(m^3)
Height	0.184	(m)
Clump Weights		
Mass	0.672	(kg)
Volume	1.1e−04	(m^3)
Height	0.02	(m)
Load Cell Description		
Mass per unit length	0.173	(kg/m)
Outer diameter	0.0015	(m)
Spring Description		
Mass per unit length	1.32	(kg/m)
Outer diameter	0.0075	(m)
Stiffness	25.33	(N/mm)
Length	0.1	(m)

Table 4
Experimental tests: definition of the regular wave conditions for the ISWEC and PeWEC case.

	ISWEC			
Wave name	T [s]	H [m]	k_λ [−]	k_d [−]
Regular Wave I01	1.230	0.079	0.033	0.551
Regular Wave I02	1.286	0.086	0.033	0.496
Regular Wave I03	1.342	0.093	0.033	0.455
	PeWEC			
Wave Name	T [s]	H [m]	k_λ [−]	k_d [−]
Regular Wave P01	1.200	0.074	0.033	0.569
Regular Wave P02	1.300	0.086	0.033	0.485
Regular Wave P03	1.400	0.099	0.033	0.418

on the ISWEC, the device kinematics were recorded using an in-board MTi and an optical Qualisys motion tracking unit. For a comprehensive understanding of the experimental campaign and associated tests, please refer to [75].

Below are the main details related to the prototype and the mooring system. Table 2 presents the hull characteristics, and Table 3 presents the mooring system characteristics.

4. Results

This section presents the results of the validation performed for both case studies. The set of wave tested in CFD are reported in Table 4. The waves are selected aiming to be representative of real site environmental conditions.[1] In Table 4, the wave period T, the wave height H, the wave steepness $k_\lambda = \frac{H}{T^2 9.81/\pi}$, and the relative water depth $k_d = \frac{wd}{T^2 9.81/\pi}$ are reported, where wd is the associated water depth fixed at 1.28 m. Please note that, for both the ISWEC and PeWEC

---

[1] The chosen waves align significantly well with the Pantelleria energy scatter (a site in southern Italy), selecting a wave steepness $k_\lambda \approx 1/30$.

cases, the three waves chosen for testing align closely with the devices resonance conditions to effectively characterize and capture the system dynamics. Therefore, although the main discussion primarily focuses on the first case scenario (*i.e.*, I01 and P01 for ISWEC and PeWEC, respectively) for space efficiency, the validation tables presented at the end of the corresponding section include all tested wave conditions.

The schematic representation of the validation process for both the ISWEC and PeWEC models is outlined in Fig. 8.

As emphasized in Section 1, a critical aspect of comprehensive validation involves the calibration of wave data. In this context, for both experimental and numerical scenarios, waves were tested without the device present to assess the undisturbed wave field.

Subsequently, the kinematics of the device are compared, as they underpin the response of the overall moored device. The validation process then examines the mooring tensions by comparing the load cell data from the model to experimental results. This step is critical since the modeling tool integrates a hydrodynamic solver with a mooring model. Finally, both experimental and numerical methods are used to define the pressure field, aiming to test the fidelity of this high-fidelity modeling tool for design cases, as also suggested in [10]. We finish by noting that, in Fig. 8, a schematic representation of the WEC is available, connecting the validation stages to the system.

4.1. ISWEC: experimental data and model validation

Within this section the results achieved by the ISWEC numerical model are compared to the corresponding experimental tests. The outcomes of the wave calibration stage are depicted in Fig. 9.

Following the wave calibration procedure detailed in Section 2.1, a good alignment with the experimental data in steady-state conditions is observed. However, in the numerical model, the wave is linearly ramped over six periods to smoothly reach steady-state conditions and prevent numerical instability. Conversely, the experimental wave exhibits a longer transient phase, leading to significant differences in the input signal until steady-state is achieved, approximately around 20 s. These discrepancies are further analyzed in terms of device kinematics, as shown in Fig. 10. While pitch and heave motions are accurately captured, a notable discrepancy is observed in surge motion.
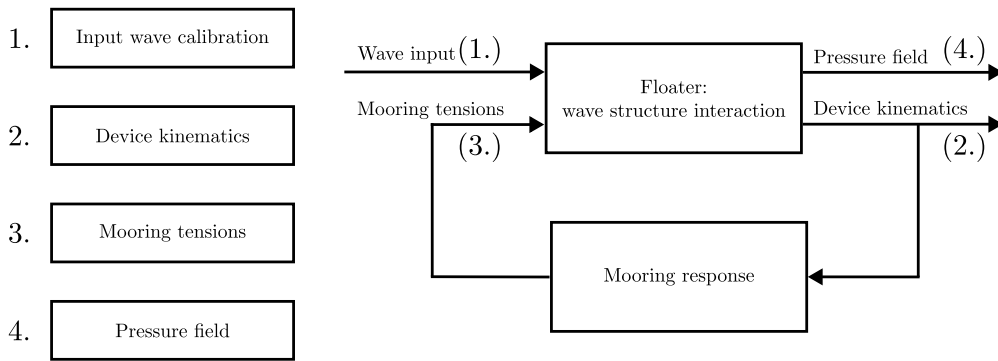
Fig. 8. Schematic representation of the validation process. The right-hand side features a diagram of the WECs, highlighting the connections with the achieved validation.
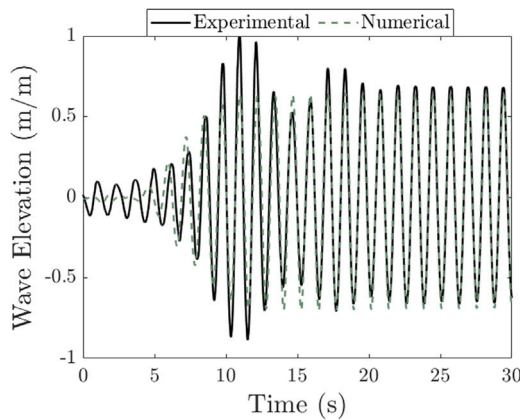

Fig. 9. Undisturbed wave elevation for Regular Wave I01 (Table 4). The numerical ramp finish time is remarked.
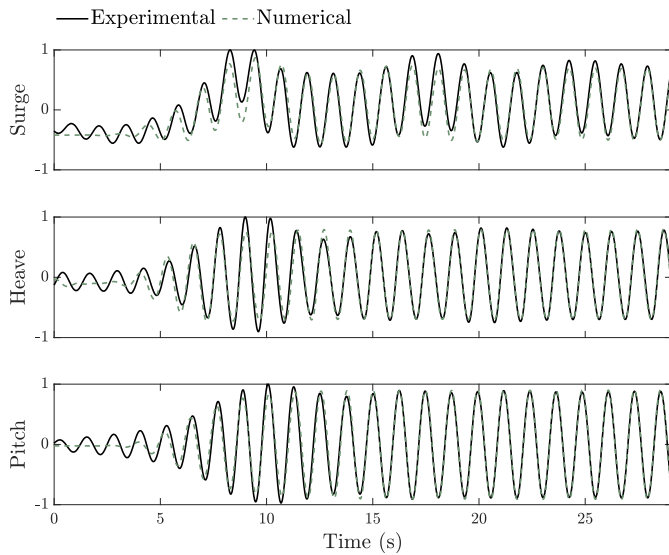

Fig. 10. Normalized pitch, surge, and heave of ISWEC for regular wave I01. Kinematic values have been normalized on the associated maximum, i.e. $\tilde{q}_i = q_i / \max(q_i)$.

The discrepancy observed during the transient phase is primarily due to significant variations in wave input between the numerical simulation and the experiment, as illustrated in Fig. 9. This behavior, albeit with less impact, is also observed in pitch and heave, where the initial discrepancies diminish quickly due to their resonant frequencies being comparable to the wave frequency. Over time, the mean

surge returns to lower values, eventually aligning with the simulation predictions after a prolonged transient phase attributed to the low resonant frequency of this DoF. The surge motion low-frequency nature is the main contributor to this phenomenon. Please note that in this study, the average of the plotted surge signal is set to zero for both ISWEC and PeWEC devices. This choice was made to facilitate a better comparison of the results for both devices after the transient conditions. When representing the WEC as a second-order Newtonian system, unlike pitch, heave, and roll motions, the remaining DoFs lack hydrostatic stiffness. Hence, all "stiffness-associated" contributions for such motions are provided by the mooring system itself. As a result, the surge transient phase significantly diminishes after the pitch and heave phases [76].

The tension analysis in the mooring lines for the ISWEC under regular wave I01 shows a good agreement with the data presented in Fig. 11. Initial discrepancies, particularly in the peak values, primarily arise from differences in wave ramping as previously discussed. Moreover, is it possible to notice a different value of the peak for the two bow line, that can be attributed to the initial position of the WEC being slightly rotated between tests before the waves start, which appears to stabilize after a couple of wave cycles, considering the significant effect of the bow-oriented wave exciting forces. It is important to highlight that, upon reaching steady-state conditions, a detailed review, particularly evident in the right-hand side of Fig. 11, indicates that the MoorDyn model is capable of closely following the experimental trend, albeit with minor variations. These differences may be attributed to the fact that, unlike in the numerical model, slight variations in line length during experimental tests can introduce asymmetries. Additionally, the polyester material stiffness exhibits nonlinear behavior, whereas the mooring model operates under the assumption of constant EA (i.e. elastic modulus multiplied by cross-sectional area). Please note that, given that the waves are oriented towards the bow and the mooring lines are symmetrically arranged, the experimental response should theoretically be symmetrical. However, due to uncertainties and minor variations, the force exerted on fairlead 2 is significantly higher than that on fairlead 1, as evidenced by the overshoot in Fig. 11.

The comparison of pressure distributions in the ISWEC simulation for regular wave I01 demonstrates that the model is able to properly represent the physical phenomena (see Fig. 12). Analyzing in details the phenomena, it is possible to appreciate that the least favorable fit occurs in the bottom section of the WEC. This discrepancy can be attributed to a calibration error in the pressure gauges offset. Furthermore, it is worth noting that although the numerical trend closely resembles the experimental one, the model pressure exhibits slight noise. This issue may stem from a mesh problem, suggesting that the mesh needs to be discretized with smaller elements to improve accuracy.

Fig. 13 displays the single-side spectrum of the pressure signals. The results are noteworthy, showing that the numerical model accurately matches the amplitudes at the wave frequency and also is able to
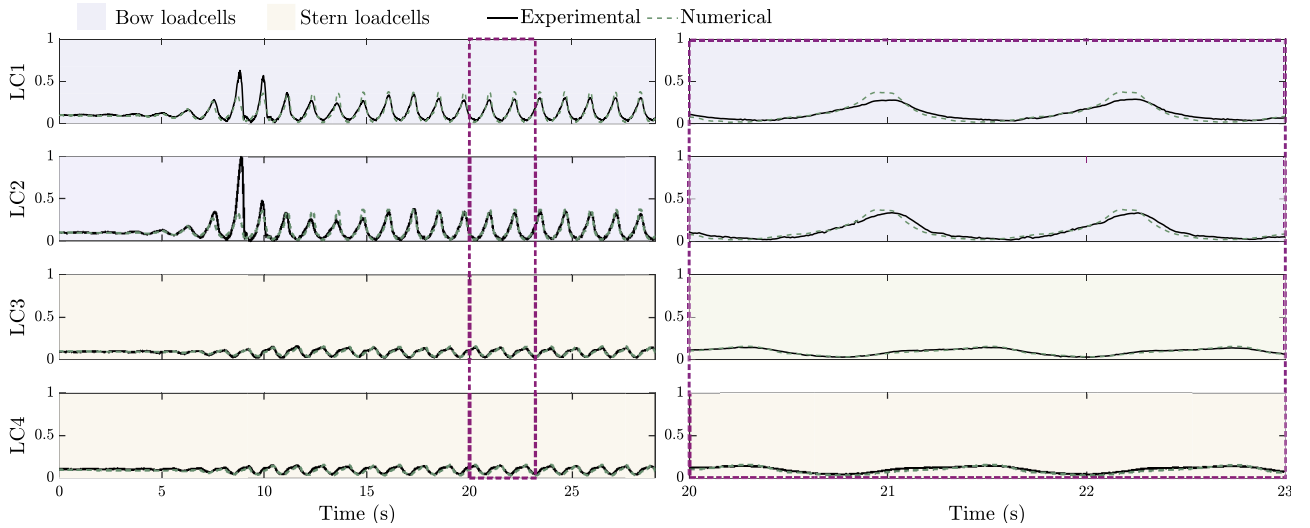
Fig. 11. Normalized mooring lines tensions of ISWEC for regular wave I01. Tension values have been normalized on the overall maximum, *i.e.* $\tilde{q}_i = q_i / \max(q)$.
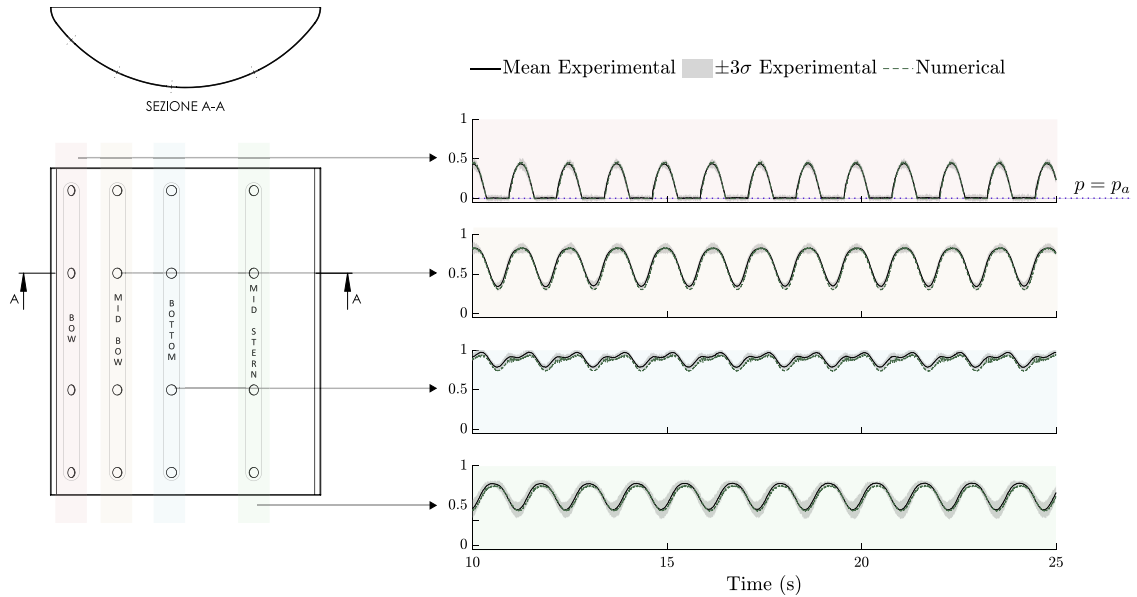

Fig. 12. Left hand-side: configuration of the ISWEC prototype featuring four rows of pressure gauges. Right hand-side: normalized pressure on ISWEC for regular wave I01. Pressure values are normalized on the overall maximum, *i.e.*, $\tilde{q}_i = q_i / \max(q)$.

represent higher order effects. This highlights that the high-frequency noise observed in the time histories does not impact the dynamic representation of the pressure on the hull. While the numerical model is able to predict the experimental response, conducting more in-depth analyses to address and mitigate this minor noise-related issue could contribute to enhancing the precision and reliability of the numerical model, particularly in regions where sensitivity is more pronounced.

We finish the ISWEC section by analyzing the model normalized mean squared error (NRMSE), which is defined as follow:

$$\text{NRMSE} = \frac{\sqrt{\frac{\sum_{i=1}^{N}(q_{1,i}-q_{2,i})^2}{N}}}{\max(q_1) - \min(q_1)}, \tag{8}$$

where $\{q_1, q_2\} : \mathbb{R}^+ \to \mathbb{R}^N, t \mapsto \{q_1(t), q_2(t)\}$ represent the experimental signal and the numerical one, respectively. Please note that, the signals cannot be normalized on the average values, since most of them are zero mean signals. Notably, the NRMSE value (Table 5) for tension is higher compared to other kinematic parameters but still falls within an acceptable range. It is noteworthy that the regular wave I02 test

presents the most significant differences, particularly in terms of surge during the transitory phase. The calculated NRMSE (Table 5) for the simulated signals present a good agreement with the experimental data. However, it is important to remark that the regular wave I02 shows relatively higher error. As previously discussed, this discrepancy can be mainly attributed to the surge motion transient. The transient wave input variations between simulation and experiment contribute to the observed differences. Despite this limitation, the surge motion overall behavior is well-represented in the simulation, and the NRMSE values, while higher, remain within acceptable limits (*i.e.* with an accuracy over the 80%).

4.2. PeWEC: experimental data and model validation

Within this section we aim to propose, as done with the ISWEC, the validation of the numerical model associated to the PeWEC device. Please note that, as discussed in Section 4.1, while the difference between the discussed device remains slight in working principle, the mooring of the PeWEC is significantly different from the ISWEC one.
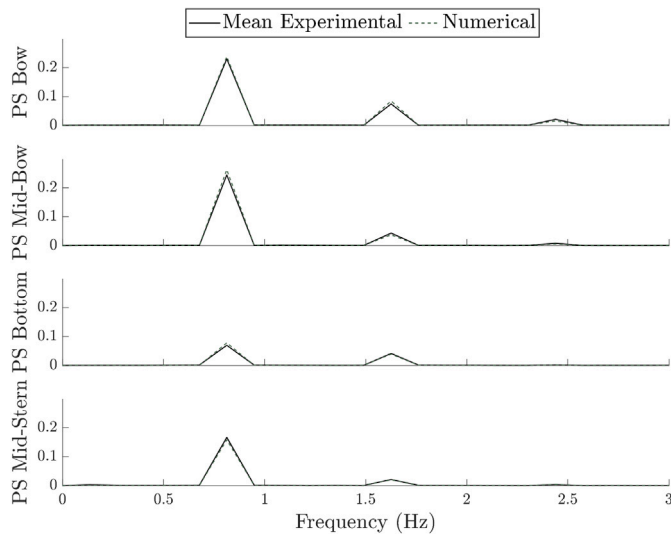
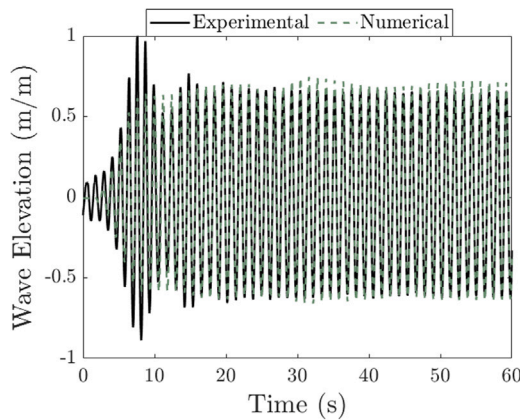**Fig. 13.** Single side spectrum of the pressure signals, after 20 s of simulation.

Fig. 14. Undisturbed wave elevation for Regular Wave P01 (Table 4). The numerical ramp finish time is remarked.

Table 5
NRMSE of ISWEC for all the waves tested, considering the signals after 20 s of beginning of test.

Signal	Reg I01	Reg I02	Reg I03
Pitch	0.013	0.030	0.021
Surge	0.053	0.083	0.178
Heave	0.012	0.018	0.028
LC1	0.117	0.139	0.113
LC2	0.067	0.087	0.153
LC3	0.087	0.108	0.135
LC4	0.140	0.162	0.183
Bow	0.038	0.036	0.056
Mid-Bow	0.065	0.081	0.066
Bottom	0.207	0.195	0.151
Mid-Stern	0.089	0.058	0.081

Indeed, a catenary mooring model, as the PeWEC one is, apply the restoring force mainly based on the lines weight. Furthermore, as the reader can notice within this section, the position of the laid line on the wave tank seabed cannot be properly reproduced within the model data (since it is linked mostly to the previous wave) and, accordingly, this aspect can influence significantly among others, the transient phase. The wave calibration results are depicted in Fig. 14, highlighting that the numerical tank successfully reproduces the experimental wave following the initial transient.
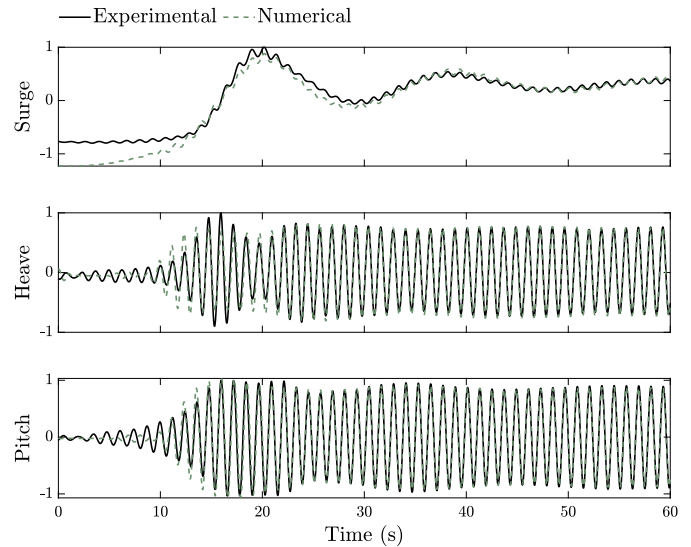

Fig. 15. Normalized pitch, surge, and heave of PeWEC for regular wave P01. Kinematic values have been normalized on the associated maximum, i.e. $\tilde{q}_i = q_i / \max(q_i)$.

In contrast to the ISWEC case study, where the prototype transient response substantially dissipates after 20 s, the PeWEC demonstrates a significantly longer transient period. This longer duration can be primarily attributed to its catenary mooring system, which provides considerably lower restoring stiffness than that of the ISWEC. As a result, to ensure the achievement of a steady-state condition, it has become necessary to extend the simulation duration. Accordingly, the simulation end time has been increased from 30 to 60 s.

The comparison between the numerical model and experimental data is illustrated in Fig. 15. Initially, a noticeable discrepancy in the surge motion initial condition is evident. This discrepancy arises partly because the equilibrium point for this system mode, dependent on both the reference frame and the equilibrium conditions used in experimental and numerical settings, is challenging to establish a priori. The experimental campaign included efforts to return PeWEC to its original design conditions post-test, involving adjustments to the mooring to mimic the initial setup. Nonetheless, manual handling of the mooring lines introduces uncertainties. Unlike the experimental setup, the numerical model consistently reproduces the initial mooring configuration. Despite these challenges and the significant influence of transient system behavior, the numerical model satisfactorily captures the overall kinematics of PeWEC, particularly in pitch and heave motions. This accuracy, even in the face of initial condition discrepancies and system transients, demonstrates the numerical model robustness in reflecting PeWEC essential kinematic characteristics. This is evidenced by the numerical model close agreement with the experimental data in steady-state conditions, typically observed after approximately 40–50 s.

Fig. 16 presents a comparison of tension signals for PeWEC, where the numerical outputs exhibit more spikes than the experimental data. This discrepancy is attributed to the high line stiffness (EA) in the catenary mooring section. The exact EA of the experimental line was not determined experimentally but was instead estimated using equations from [77]. For clarity, the numerical stiffness was reduced from its original scaled value due to the numerical simulation being affected by resonance in the line segments. To address this issue and decrease numerical noise, the EA value has been changed by still respecting the order of magnitude, as long the restoring force in a catenary mooring system is still primarily due to the weight of the catenary. Additionally, the dynamics of the catenary system, unlike the ISWEC mooring system, must account for the friction between the line and the wave tank seabed. This aspect is particularly challenging to evaluate
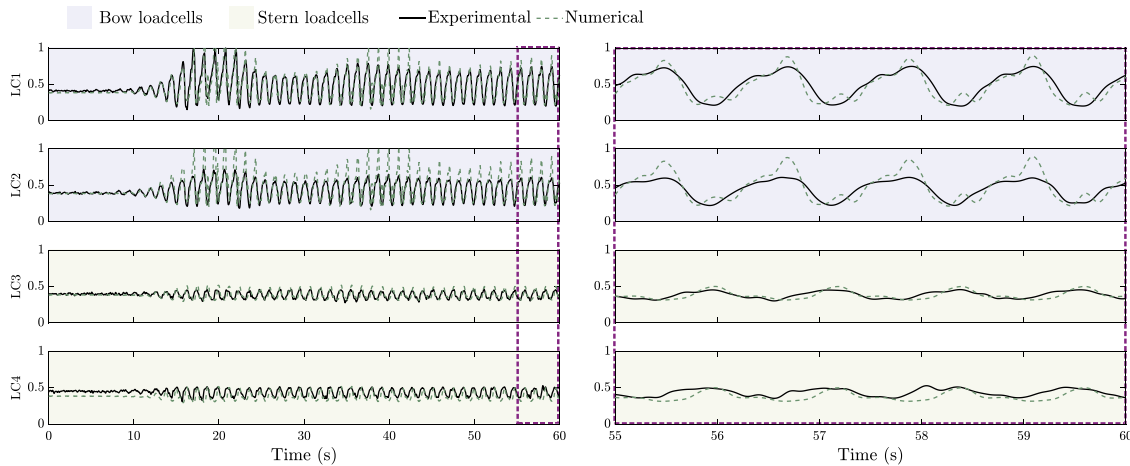
Fig. 16. Normalized mooring lines tensions of PeWEC for regular wave P01. Tension values have been normalized on the overall maximum, *i.e.* $\tilde{q}_i = q_i / \max(q)$.

Table 6
NRMSE of PeWEC for all the waves tested, considering the signals after 40 s of beginning of the test.

Signal	Reg P01	Reg P02	Reg P03
Pitch	0.014	0.036	0.042
Surge	0.131	0.215	0.160
Heave	0.020	0.026	0.029
LC1	0.159	0.194	0.112
LC2	0.263	0.108	0.125
LC3	0.225	0.162	0.148
LC4	0.191	0.121	0.185
Bow	0.081	0.102	0.109
Mid-Bow	0.056	0.081	0.092
Bottom	0.372	0.274	0.407
Mid-Stern	0.162	0.102	0.081
Stern	0.185	0.177	0.207

in experimental setups and adds complexity to accurately representing catenary dynamics.

In the PeWEC case study, pressure signals were compared using data from five rows of three pressure gauges each, as depicted in Fig. 17. Though the overall trend is well captured, slight discrepancies in the mean values are observed, particularly for the bow, bottom, and stern sections. This discrepancy is attributed to an error in the offset of the pressure probes used in the experimental setup. This assumption is supported by the pressure values of the experimental probes above the waterline. Considering that the reference signal for the pressure is the atmospheric one, if the gauges are properly calibrated, the signal from the pressure probe should be equal to 0 when the probe is out of water, as accurately reflected in the numerical model. However, in the experimental setup, the readings deviate from 0, indicating an incorrect offset value for these specific probes. This difference in mean values does not compromise the overall agreement between the simulation and experimental data, as the dynamic behavior and trends in the pressure signals align well. Fig. 18 shows the single-sided spectrum of the pressure signals. The numerical model accurately captures the dynamic behavior of the pressure on the hull. Upon closer examination of Fig. 18, it becomes evident that in the vicinity of the wave frequency, smaller and higher frequencies are also present, albeit with smaller amplitudes. This phenomenon is attributed to the Doppler effect induced by the surge, which is significantly higher in PeWEC compared to ISWEC due to the different mooring setup.

The high-fidelity tool effectively captures the PeWEC motion (see Table 6). However, while the overall kinematics are well described by the numerical model, surge motions remain the most challenging phenomena to characterize. This challenge arises from the difficulty in accurately representing the transition phase and the initial conditions

of the experimental mooring, which inherently differ from those in the numerical model. Slight discrepancies in mean pressure values result from an offset error in the experimental probes.

5. Conclusion

In the field of wave energy applications, the necessity of high-fidelity models to accurately capture nonlinear phenomena is undeniable. However, these models often fall short when it comes to accurately representing the complexities of moored floating bodies, especially in the absence of considerations for mooring systems. To bridge this critical gap and facilitate the design-oriented utilization of high-fidelity models, this study details the development and validation of a coupling mechanism between Star CCm+ and MoorDyn.

Validation of the developed coupling was conducted utilizing data from two experimental campaigns, featuring ISWEC and PeWEC as case studies. The results exhibit satisfactory agreement between numerical predictions and experimental observations. Notably, the versatility of the coupling mechanism is showcased in its ability to model both semi-taut and catenary mooring systems effectively. The model demonstrates proficiency in accurately predicting kinematics, mooring tension, and hull pressure for floating bodies. While linear-based software may suffice in reproducing device responses under specific conditions, such as small waves, they invariably fall short in replicating the pressure fields around the device. Moreover, their limitations become pronounced in harsh environmental conditions, when nonlinear effects are more pronounced.

The capacity to faithfully reproduce the pressure field stands as a pivotal feature of high-fidelity models, underscoring their significance in both the design phase, where they afford a comprehensive perspective of the pressure field, and in the validation of models across diverse environmental scenarios, including the relevant mooring effect.

The developed coupling is publicly accessible online link, where readers can access a simplified case study. By releasing this coupling to the public domain, we aim to make a meaningful contribution to the research field and encourage others to adopt this methodology for their studies.

In conclusion, we acknowledge the inherent limitations of the numerical model. Representing a polyester line with constant axial stiffness is a simplification that necessitates addressing in future work, as current constraints within MoorDyn prohibit the representation of non-constant axial stiffness. Additionally, future work will focus on simulating short-duration irregular wave series, such as focused and multisine waves, which are computationally feasible with a high-fidelity model and provide more realistic sea state conditions.
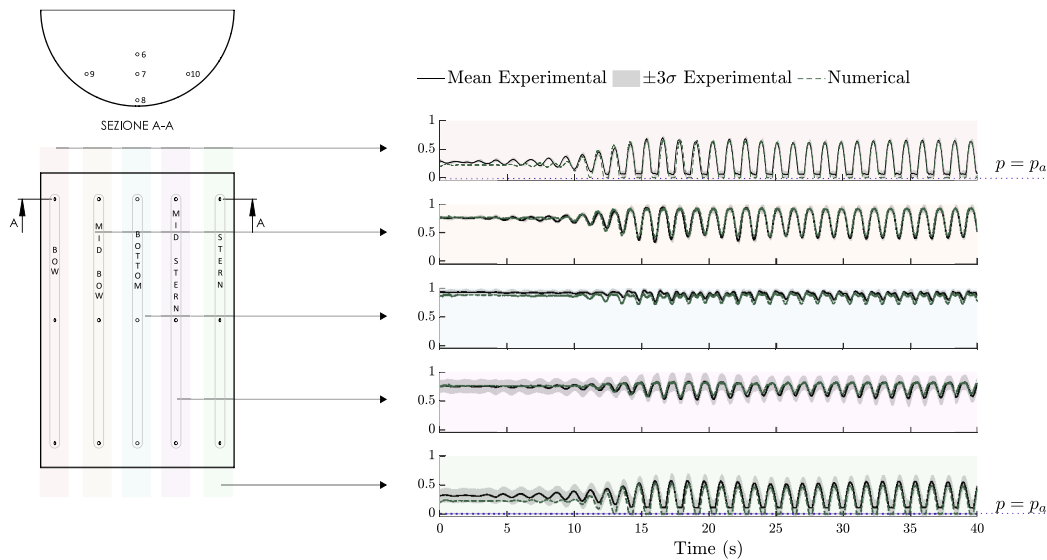
Fig. 17. Left hand-side: configuration of the PeWEC prototype featuring five rows of pressure gauges. Right hand-side: normalized pressure on PeWEC for regular wave P01. Pressure values are normalized on the overall maximum, *i.e.*, $\tilde{q}_i = q_i / \max(q)$.
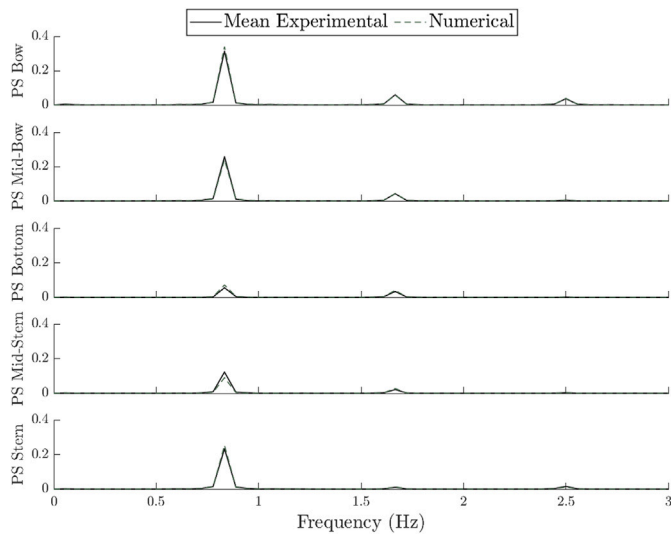

Fig. 18. Single side spectrum of the pressure signals, after 40 s of simulation.

Data statement

The ISWEC experimental campaign was funded by Eni spa for commercial investigation purposes regarding the prototype. Therefore, the device properties as well as the mooring configuration cannot be disclosure in this manuscript. Also, motions are expressed in a dimensionless form. To maintain consistency in the presentation of the case studies, the same approach has been adopted for the PeWEC device. Specifically, the maximum value from the experimental campaign was used as the normalization factor. For tension measurements, the highest value recorded by any of the load cells across all signals was selected as the normalization reference. This approach ensures that the differences between the mooring tensions are clearly visible. Similarly, for the pressure signals, the highest experimental value was used for normalization. This method allows for a consistent basis of comparison.

The interface files, for MoorDyn Star CCm+ coupling, are uploaded on https://github.com/OronzoD/STAR-MoorDyn-Coupling and are available to be downloaded for any user. Additionally, a simplified case study is provided, which includes a floating sphere moored by a semi-taut mooring system.

CRediT authorship contribution statement

Oronzo Dell'Edera: Writing – original draft, Visualization, Validation, Software, Methodology, Investigation, Formal analysis, Data curation. **Francesco Niosi:** Writing – original draft, Visualization, Validation, Formal analysis, Data curation. **Pietro Casalone:** Software, Methodology, Data curation. **Mauro Bonfanti:** Supervision, Project administration, Data curation. **Bruno Paduano:** Writing – review & editing, Writing – original draft, Visualization, Supervision. **Giuliana Mattiazzo:** Supervision, Resources, Project administration.

Declaration of competing interest

The authors declare that they have no known competing financial interests or personal relationships that could have appeared to influence the work reported in this paper.

Data availability

The data that has been used is confidential.

Declaration of Generative AI and AI-assisted technologies in the writing process

During the preparation of this work the authors used ChatGPT-3.5 in order to improve the readability of the paper. After using this tool, the authors reviewed and edited the content as needed and take full responsibility for the content of the publication.
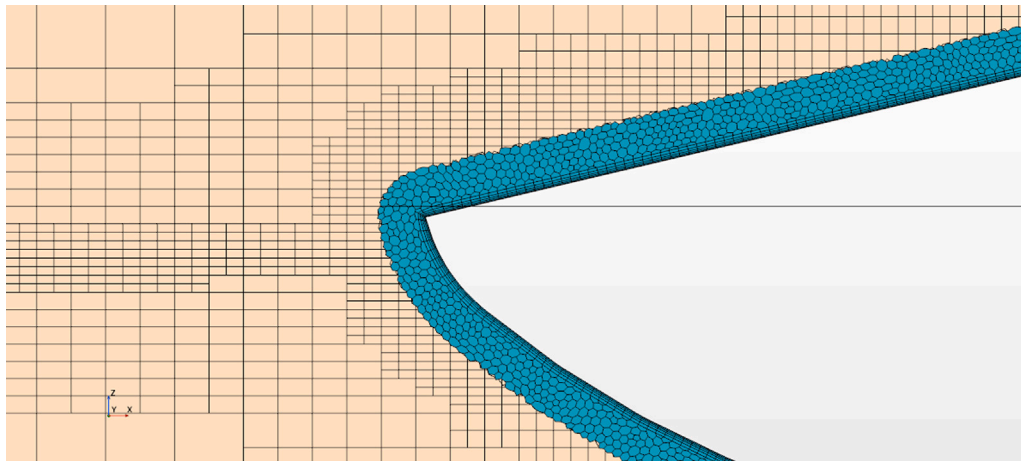
Acknowledgments

Fig. A.19. In beige the Numerical Wave Tank. In blue the overset mesh. The cells at the interface between the two regions has comparable size to reduce interpolation errors.

Table A.7
Key parameter of the mesh.

Symbol	Meaning
H	Wave Height
N	Number of cells per wave height
u	Minimum allowable size of the mesh: $\frac{H}{N}$
Ar_x	Aspect Ratio in the X direction
Ar_y	Aspect Ratio in the Y direction

Appendix. Technical note

In the simulation framework, the computational domain is divided into two regions: tank and overset. The tank represents a virtual portion of the sea, and the overset zone encloses the geometry of the hull. The overset mesh Fig. A.19 approach enables the movement of the body without the need for remeshing, thanks to the dynamic fluid-body interaction (DFBI) model [78,79]. Please note that, the mesh definition is a fundamental step to represent properly the wave transport and the associated hydrodynamic loads. In the tank region, a trimmed mesh configuration is employed with key parameters defined in Table A.7.

There are two main volume refinements in the tank region. The first, known as the "sea refinement", is employed to define a region between $[H, -H]$. The second refinement, called the "overset refinement", is situated around the overset region. and it aims to facilitate better information exchange between the overset and the tank. Additionally, to minimize the size of the overset refinement, the wave tank match the surge motion of the body, ensuring the device remains centrally positioned within the wave tank. After generating the mesh, every 10 time steps trigger a refinement at the interface between the overset and tank regions, as well as at the free surface. This refinement process is managed by the AMR, allowing for a division of the cell size in each dimension by a factor of 4. A transition width, equal to 6, is defined to gradually increase cell sizes, preventing the propagation of reflections. After the AMR, the cell size at the free surface becomes u in the z direction, $2u$ in the x direction, and either $4u$ or $2u$ in the y direction, depending on whether the cell is inside or outside the overset refinement. In Fig. A.20 is reported a volume fraction scene with the mesh of a section of the wave tank before and after the AMR.

The AMR is a must use in Star CCm+ as it allows to heavily reduce computational cost. In the current case, the total cell count dropped from 9–11 million cells to 5–6 million cells (depending on the wave simulated) while ensuring the same accuracy [80]. The time required for the refinement to take place is negligible in respect to the solver computational time for a time step. However, it should be noted that achieving consistent and reliable convergence of flow solvers or residuals remains a challenge in many industrial cases, as highlighted

Table A.8
Principal characteristics of the mesh in the Tank region. The cell size dimensions refers to the size before AMR.

Trimmed Mesh Characteristics	
N	16
Minimum cell size	u
Maximum cell size	32u
Total cell number	5-6 M
Sea Refinement	
Z cell size	4u
X cell size	8u
Y cell size	16u
Overset Refinement	
Z cell size	4u
X cell size	8u
Y cell size	8u
AMR setup	
Max refinement levels	2
Transition width	6
Trigger	10 time steps

Table A.9
Principal characteristics of the mesh in the Overset region.

Polyhedral Mesh Characteristics	
Minimum cell size	u
Maximum cell size	2u
Total cell number	0.5 M
Target Surface Size	u
Volume Grow Rate	1.15
Prism layer Characteristics	
Y+ target	50
N layers	6
Grow Rate	1.2

in [80]. In Table A.8 are reported the principal characteristic of the tank mesh.

For the overset region a polyhedral mesh is used to better capture the geometry of the body combined with a prism layer mesher, that enables the creation of a easier way to discretize the boundary layer. The overset region has been defined performing an offset of the body, ensuring that, prism layer excluded, there are at least 6 cell between the overset interface and the body surface. The principal characteristic of the overset mesh are reported in Table A.9.

To establish the problem, it is necessary to apply boundary conditions to the domain. These conditions are specified on the external surfaces of the domain. Fig. A.21 illustrates the boundary conditions
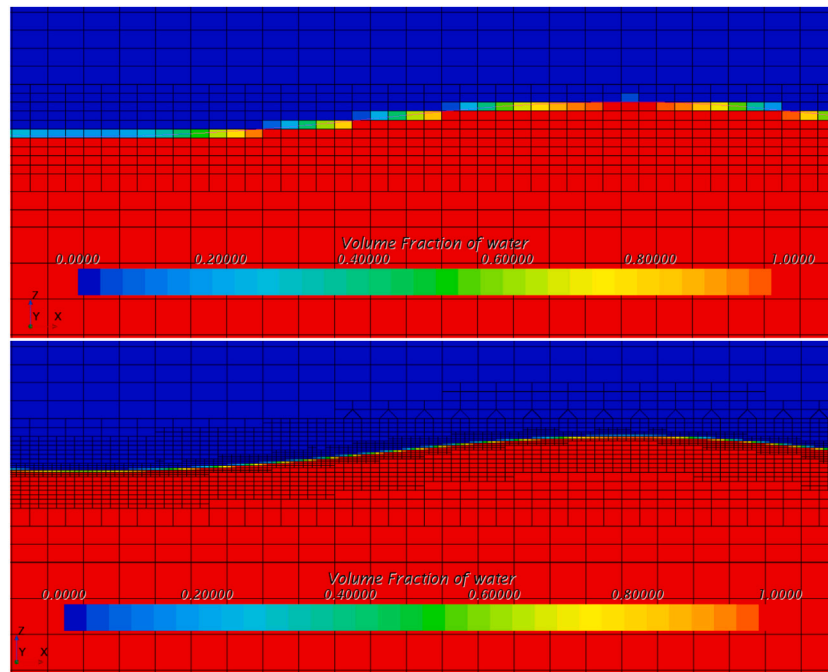
Fig. A.20. Volume fraction of water: on the top before AMR, on the bottom the same portion of space after AMR.

at the tank's perimeter. The inlet, outlet, and side boundaries function as velocity inlets, where the fluid's quantity entering and leaving the domain, along with the associated momentum and volume fraction, is imposed. Additionally, a forcing zone is defined for this boundaries to reduce potential reflection, and the reflection coefficient is set as suggested by Peric et al. [81]. The forcing zone is 2λ for the inlet and outlet and 1λ for the side. In the forcing zone the numerical solution for the momentum is partially corrected with the theoretical momentum of the particles. The correction follow a cos^2 function being equal to 1 at the boundary and equal to 0 at the end of the forcing zone. The bottom boundary is modeled as a slip wall. The top is designated as a pressure outlet, allowing for the adjustment of static pressure. The simulation exhibits symmetry with respect to the $y = 0$ surface. The external surface of the overset volume is assigned a mesh interface as its boundary condition. This configuration allows the interaction and information exchange between the two regions.

For wave generation, a 5th-order Stokes wave, already integrated into the VOF waves module of Star CCm+, has been used [82]. The waves propagate under deep-water approximations, as the depth significantly exceeds the wavelength for the given test cases. The accurate transport of waves relies on an appropriately chosen time step. This was chosen to ensure that the maximum CFL (Courant–Friedrichs–Lewy) number is approximately 0.2 for the cells at the free surface in the wave tank. It has been confirmed through verification that a higher time step is linked to a pronounced spatial decay of the wave outside the forcing zone. Specifically, with a CFL number around 0.3, at least 10% of the wave height is lost, and when the CFL is approximately 0.5, the spatial damping becomes more significant, leading to waves being out of phase [83]. To satisfy this condition, for test I01, a time step of 0.0016s was used. Note that the time step used for other tests is close to this value but differs slightly to maintain a maximum CFL of approximately 0.2 and a mean CFL at the free surface of 0.1 (see Fig. A.22).

Table A.10 presents the grid convergence test performed on the ISWEC for test case I01. The Base Size (BS) parameter represents the scaling percentage of the minimum cell size u used in the mesh. For example, a BS of 100 corresponds to 100% of the described cell size. For this study, 4 BS has been tested. Initially, we expected the total cell count to scale by a factor of $1.25^3 \approx 1.95$, as 1.25 is the

Table A.10
The transfer function for the input wave was adjusted for each test to ensure the correct wave excites the device. The CFL number was kept constant throughout the study. These values refers to the test I01.

Base size	Tank N° of cells	Overset N° of cells
156	2.1M	0.19M
125	3.3M	0.31M
100	5.2M	0.50M
80	8.6M	0.82M

Table A.11
NRMSE of ISWEC for the BS considered in the grid convergence.

Signal	Bs 80	Bs 100	Bs 125	Bs 156
Pitch	0.016	0.013	0.009	0.022
Surge	0.053	0.053	0.056	0.065
Heave	0.020	0.020	0.021	0.032

Table A.12
RMS of ISWEC for the BS considered in the grid convergence.

Signal	Bs 80	Bs 100	Bs 125	Bs 156
Pitch	0.644	0.637	0.623	0.584
Surge	0.0422	0.0417	0.0407	0.0379
Heave	0.533	0.528	0.518	0.488

ratio between consecutive BS values. However, the actual observed ratio was approximately 1.65. This discrepancy occurs because the transition width of the AMR determines a fixed number of cells before the mesh size increases, independent of BS. Consequently, for smaller BS values, the transition width in volume is reduced, leading to a lower-than-expected total cell count ratio.

For BS values smaller than 125, the differences in the kinematics of the device, as shown in Fig. A.23, are minimal. Thus, a BS of 100 was chosen as an optimal balance between computational cost and accuracy. It should be noted that in this analysis the CFL was kept constant, so the time step was also scaled. For the final setup, simulating 1 s of runtime requires ~95 min on a HPC. This setup utilizes 10 nodes, each with 2 CPUs, each CPU having 24 cores (AMD
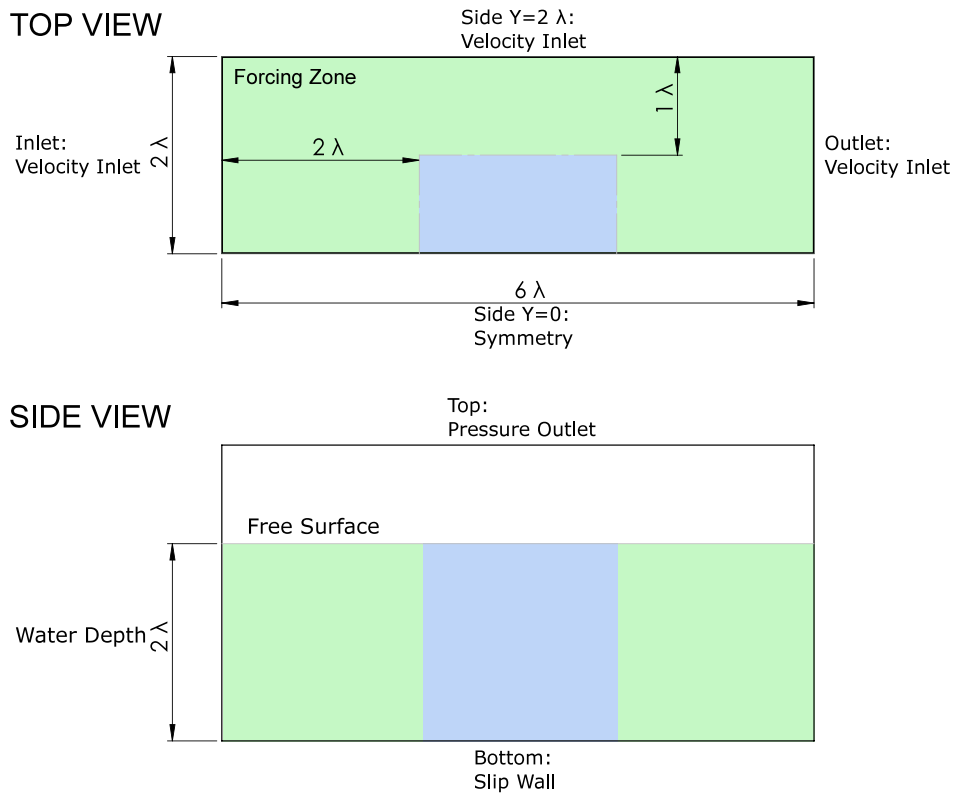
Fig. A.21. Domain dimensions and boundaries definition in top and side views. The forcing zone is in green and the fully resolve U-RANS are in blue.
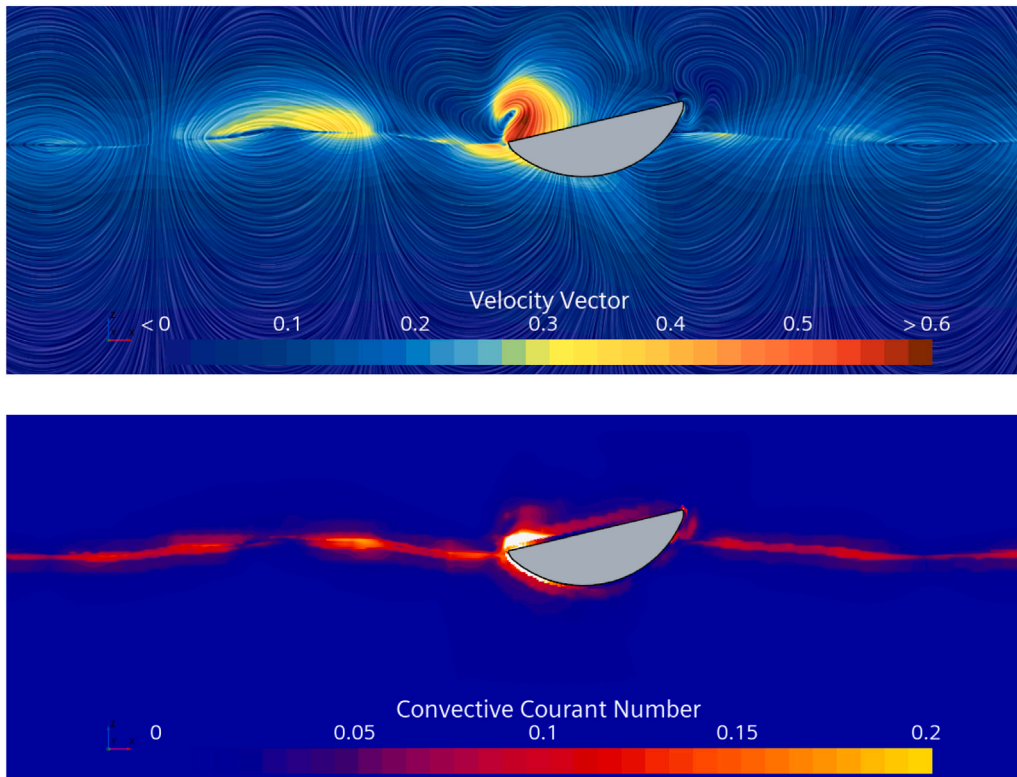

Fig. A.22. On the top the velocity vector during a simulation. On the bottom the CFL. At the free surface the CFL is always less than 0.2.
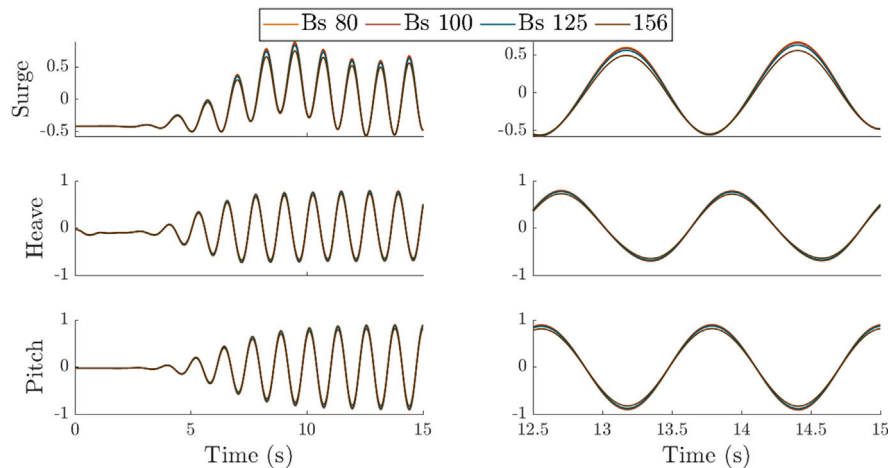
Fig. A.23. On the left, the kinematics of ISWEC for the four base sizes tested. On the right, the last two wave periods are shown to highlight the differences between each test.

second-generation Epyc Rome 24-core 7402), totaling 480 cores (see Tables A.11 and A.12) .

References

[1] González AT, Dunning P, Howard I, McKee K, Wiercigroch M. Is wave energy untapped potential? Int J Mech Sci 2021;205:106544. http://dx.doi.org/10.1016/j.ijmecsci.2021.106544.

[2] Ilyas A, Kashif SA, Saqib MA, Asad MM. Wave electrical energy systems: Implementation, challenges and environmental issues. Renew Sustain Energy Rev 2014;40:260–8. http://dx.doi.org/10.1016/j.rser.2014.07.085.

[3] Magagna D. Ocean energy: Technology market report. EUR 29924 EN, Luxembourg: Publications Office of the European Union; 2019, http://dx.doi.org/10.2760/852200, JRC118311.

[4] Cruz J. Ocean wave energy: Current status and future prespectives. 2008, http://dx.doi.org/10.1007/978-3-540-74895-3.

[5] Lewis A, Estefen S, Huckerby J, Musial W, Pontes T, Torres-Martinez J. Ocean energy. In: Edenhofer O, Pichs-Madruga R, Sokona Y, Seyboth K, Matschoss P, Kadner S, Zwickel T, Eickemeier P, Hansen G, Schlömer S, von Stechow C, editors. IPCC special report on renewable energy sources and climate change mitigation. Cambridge/New York: Cambridge University Press; 2011, p. 497–533.

[6] Bonfanti M, Giorgi G. Improving computational efficiency in WEC design: Spectral-domain modelling in techno-economic optimization. J Mar Sci Eng 2022;10(10):1468. http://dx.doi.org/10.3390/jmse10101468.

[7] Coe RG, Rosenberg BJ, Quon EW, Chartrand CC, Yu Y-H, van Rij J, et al. CFD design-load analysis of a two-body wave energy converter. J Ocean Eng Mar Energy 2019;5:99–117. http://dx.doi.org/10.1007/s40722-019-00129-8.

[8] Niosi F, Dell'Edera O, Sirigu M, Ghigo A, Bracco G. A comparison between different numerical models and experimental tests for the study of floating offshore wind turbines. In: ISOPE international ocean and polar engineering conference. ISOPE; 2023, p. ISOPE–I.

[9] Dell'Edera O, Casalone P, Giorgi G. Influence of the energy extraction system on the kinematics of a WEC: High-fidelity CFD with mooring and power extraction co-simulation. In: 2022 international conference on electrical, computer, communications and mechatronics engineering. IEEE; 2022, p. 1–6. http://dx.doi.org/10.1109/ICECCME55909.2022.9988179.

[10] Paduano B, Parrinello L, Niosi F, Dell'Edera O, Sirigu SA, Faedo N, et al. Towards standardised design of wave energy converters: A high-fidelity modelling approach. Renew Energy 2024;224:120141. http://dx.doi.org/10.1016/j.renene.2024.120141.

[11] Li G, Stansby P, Draycott S. General formulation for floating body with elastic mooring in irregular waves: A hybrid linear and nonlinear framework and validation. Mar Struct 2024;96:103623. http://dx.doi.org/10.1016/j.marstruc.2024.103623.

[12] Niosi F, Dell'Edera O, Dutto L, Bracco G. A comparison between different numerical models and experimental tests for the study of floating offshore wind turbines. Int J Offshore Polar Eng (IJOPE) 2024. [submitted for publication].

[13] Windt C, Davidson J, Ringwood JV. High-fidelity numerical modelling of ocean wave energy systems: A review of computational fluid dynamics-based numerical wave tanks. Renew Sustain Energy Rev 2018;93:610–30. http://dx.doi.org/10.1016/j.rser.2018.05.020.

[14] DNV. DNV-OS-E301 Position mooring. 2015, URL www.dnvgl.com.

[15] IEC. IEC TS 62600-10. 2019.

[16] DNV. Environmental conditions and environmental loads. 2019, URL https://www.dnv.com/oilgas/download/dnv-rp-c205-environmental-conditions-and-environmental-loads.html.

[17] Xu S, Wang S, Soares CG. Review of mooring design for floating wave energy converters. Renew Sustain Energy Rev 2019;111:595–621. http://dx.doi.org/10.1016/j.rser.2019.05.027.

[18] Johanning L, Smith GH, Wolfran J. Mooring design approach for wave energy converters. J Eng Marit Environ 2006;220:159–74.

[19] Fitzgerald J, Bergdahl L. Including moorings in the assessment of a generic offshore wave energy converter: A frequency domain approach. Mar Struct 2008;21:23–46. http://dx.doi.org/10.1016/j.marstruc.2007.09.004.

[20] Cerveira F, Fonseca N, Pascoal R. Mooring system influence on the efficiency of wave energy converters. Int J Mar Energy 2013;3–4:65–81. http://dx.doi.org/10.1016/J.IJOME.2013.11.006.

[21] Paduano B, Pasta E, Papini G, Carapellese F, Bracco G. Mooring influence on the productivity of a pitching wave energy converter. 2021, p. 1–6. http://dx.doi.org/10.23919/oceans44145.2021.9706108,

[22] Niosi F, Parrinello L, Paduano B, Pasta E, Carapellese F, Bracco G. On the influence of mooring in wave energy converters productivity: the PeWEC case. In: 2021 International conference on electrical, computer, communications and mechatronics engineering. 2021, p. 1–6. http://dx.doi.org/10.1109/ICECCME52200.2021.9590867.

[23] Gubesch E, Abdussamie N, Penesis I, Chin C. Effects of mooring configurations on the hydrodynamic performance of a floating offshore oscillating water column wave energy converter. Renew Sustain Energy Rev 2022;166:112643. http://dx.doi.org/10.1016/J.RSER.2022.112643.

[24] Qiao D, Haider R, Yan J, Ning D, Li B. Review of wave energy converter and design of mooring system. Sustainability 2020;12(19):8251. http://dx.doi.org/10.3390/su12198251.

[25] Paduano B, Carapellese F, Pasta E, Sergej S, Faedo N, Mattiazzo G. Data-based control synthesis and performance assessment for moored wave energy conversion systems: the PeWEC case. IEEE Trans Sustain Energy 2023. http://dx.doi.org/10.1109/TSTE.2023.3285016.

[26] Paduano B, Carapellese F, Pasta E, Faedo N, Mattiazzo G. Optimal controller tuning for a nonlinear moored wave energy converter via non-parametric frequency-domain techniques. 2022, http://dx.doi.org/10.1201/9781003360773-45,

[27] Bhinder M, Karimirad M, Weller S, Debruyne Y, Guerinel M, Sheng W. Modelling mooring line non-linearities (material and geometric effects) for a wave energy converter using AQWA, SIMA and orcaflex. In: Proceedings of the 11th European wave and tidal energy conference. 2015, URL https://www.researchgate.net/publication/282574165_Modelling_mooring_line_non-linearities_material_and_geometric_effects_for_a_wave_energy_converter_using_AQWA_SIMA_and_Orcaflex.

[28] Depalo F, Wang S, Xu S, Soares CG. Design and analysis of a mooring system for a wave energy converter. J Mar Sci Eng 2021;9. http://dx.doi.org/10.3390/jmse9070782.

[29] Mao Y, Wang T, Duan M. A DNN-based approach to predict dynamic mooring tensions for semi-submersible platform under a mooring line failure condition. Ocean Eng 2022;266:112767. http://dx.doi.org/10.1016/J.OCEANENG.2022.112767.

[30] Wei H, Xiao L, Liu M, Kou Y. Data-driven model and key features based on supervised learning for truncation design of mooring and riser system. Ocean Eng 2021;224:108743. http://dx.doi.org/10.1016/J.OCEANENG.2021.108743.

[31] Tran TT, Kim D-H. Fully coupled aero-hydrodynamic analysis of a semi-submersible fowt using a dynamic fluid body interaction approach. Renew Energy 2016;92:244–61. http://dx.doi.org/10.1016/j.renene.2016.02.021.

[32] Zhang Y, Kim B. A fully coupled computational fluid dynamics method for analysis of semi-submersible floating offshore wind turbines under wind-wave excitation conditions based on OC5 data. Appl Sci 2018;8(11):2314. http://dx.doi.org/10.3390/app8112314.

[33] Cheng P, Huang Y, Wan D. A numerical model for fully coupled aero-hydrodynamic analysis of floating offshore wind turbine. Ocean Eng 2019;173:183–96. http://dx.doi.org/10.1016/j.oceaneng.2018.12.021.

[34] Liu Y, Xiao Q, Incecik A, Peyrard C, Wan D. Establishing a fully coupled CFD analysis tool for floating offshore wind turbine. Renew Energy 2017;112:280–301. http://dx.doi.org/10.1016/j.renene.2017.04.052.

[35] Hall M, Buckham B, Crawford C. Evaluating the importance of mooring line model fidelity in floating offshore wind turbine simulations. Wind Energy 2014;17(12):1835–53. http://dx.doi.org/10.1002/we.1669.

[36] Chen H, Hall M. CFD simulation of floating body motion with mooring dynamics: Coupling MoorDyn with OpenFOAM. Appl Ocean Res 2022;124:103210. http://dx.doi.org/10.1016/j.apor.2022.103210.

[37] Lee SC, Song S, Park S. Platform motions and mooring system coupled solver for a moored floating platform in a wave. Processes 2021;9(8):1393. http://dx.doi.org/10.3390/pr9081393.

[38] Palm J, Eskilsson C, Paredes GM, Bergdahl L. Coupled mooring analysis for floating wave energy converters using CFD: Formulation and validation. Int J Mar Energy 2016;16:83–99. http://dx.doi.org/10.1016/j.ijome.2016.05.003.

[39] Eskilsson C, Palm J. High-fidelity modelling of moored marine structures: multi-component simulations and fluid-mooring coupling. J Ocean Eng Mar Energy 2022;8(4):513–26. http://dx.doi.org/10.1007/s40722-022-00263-w.

[40] Aliyar S, Ducrozet G, Bouscasse B, Bonnefoy F, Sriram V, Ferrant P. Numerical coupling strategy using HOS-OpenFOAM-MoorDyn for OC3 Hywind SPAR type platform. Ocean Eng 2022;263:112206. http://dx.doi.org/10.1016/j.oceaneng.2022.112206.

[41] Xi K, Milne IA, Draper S, Chen L. On the application of overset meshing to numerical studies of roll damping of hulls in complex scenarios. Ocean Eng 2023;290:116173. http://dx.doi.org/10.1016/j.oceaneng.2023.116173.

[42] Windt C, Davidson J, Akram B, Ringwood JV. Performance assessment of the overset grid method for numerical wave tank experiments in the openfoam environment. In: International conference on offshore mechanics and arctic engineering, vol. 51319. American Society of Mechanical Engineers; 2018, V010T09A006. http://dx.doi.org/10.1115/OMAE2018-77564.

[43] Katsidoniotaki E, Göteman M. Numerical modeling of extreme wave interaction with point-absorber using OpenFOAM. Ocean Eng 2022;245:110268. http://dx.doi.org/10.1016/j.oceaneng.2021.110268.

[44] Chen H, Qian L, Cao D. Analysis of convergence behavior for the overset mesh based numerical wave tank in OpenFOAM. In: International conference on offshore mechanics and arctic engineering, vol. 86892. American Society of Mechanical Engineers; 2023, V007T08A041. http://dx.doi.org/10.1115/OMAE2023-104586.

[45] Windt C, Davidson J, Chandar DD, Faedo N, Ringwood JV. Evaluation of the overset grid method for control studies of wave energy converters in OpenFOAM numerical wave tanks. J Ocean Eng Mar Energy 2020;6(1):55–70. http://dx.doi.org/10.1007/s40722-019-00156-5.

[46] Katsidoniotaki E, Shahroozi Z, Eskilsson C, Palm J, Engström J, Göteman M. Validation of a CFD model for wave energy system dynamics in extreme waves. Ocean Eng 2023;268:113320. http://dx.doi.org/10.1016/j.oceaneng.2022.113320.

[47] Crespo AJ, Hall M, Domínguez JM, Altomare C, Wu M, Verbrugghe T, et al. Floating moored oscillating water column with meshless SPH method. In: International conference on offshore mechanics and arctic engineering. 51333, American Society of Mechanical Engineers; 2018, V11BT12A053. http://dx.doi.org/10.1115/OMAE2018-77313.

[48] Domínguez JM, Crespo AJ, Hall M, Altomare C, Wu M, Stratigaki V, et al. SPH simulation of floating structures with moorings. Coast Eng 2019;153:103560. http://dx.doi.org/10.1016/j.coastaleng.2019.103560.

[49] Lyu H-G, Sun P-N, Huang X-T, Zhong S-Y, Peng Y-X, Jiang T, et al. A review of SPH techniques for hydrodynamic simulations of ocean energy devices. Energies 2022;15(2):502. http://dx.doi.org/10.3390/en15020502.

[50] Lind SJ, Rogers BD, Stansby PK. Review of smoothed particle hydrodynamics: towards converged Lagrangian flow modelling. Proc R Soc A 2020;476(2241):20190801. http://dx.doi.org/10.1098/rspa.2019.0801.

[51] Tagliafierro B, Karimirad M, Martínez-Estévez I, Domínguez JM, Viccione G, Crespo AJ. Numerical assessment of a tension-leg platform wind turbine in intermediate water using the smoothed particle hydrodynamics method. Energies 2022;15(11):3993. http://dx.doi.org/10.3390/en15113993.

[52] Tagliafierro B, Karimirad M, Altomare C, Göteman M, Martínez-Estévez I, Capasso S, et al. Numerical validations and investigation of a semi-submersible floating offshore wind turbine platform interacting with ocean waves using an SPH framework. Appl Ocean Res 2023;141:103757. http://dx.doi.org/10.1016/j.apor.2023.103757.

[53] Chen Q, Zang J, Ning D, Blenkinsopp C, Gao J. A 3D parallel particle-in-cell solver for extreme wave interaction with floating bodies. Ocean Eng 2019;179:1–12. http://dx.doi.org/10.1016/j.oceaneng.2019.02.047.

[54] Ransley EJ, Brown SA, Hann M, Greaves DM, Windt C, Ringwood J, et al. Focused wave interactions with floating structures: A blind comparative study. Proc Inst Civ Eng-Eng Comput Mech 2021;174(1):46–61. http://dx.doi.org/10.1680/jencm.20.00006.

[55] Paduano B, Carapellese F, Pasta E, Bonfanti M, Sirigu S, Basile D, et al. Experimental and numerical investigation on the performance of a moored pitching wave energy conversion system. IEEE J Ocean Eng 2024. http://dx.doi.org/10.1109/JOE.2024.3353372.

[56] Baran O. Simulating mooring lines or cables with DEM fiber in simcenter STAR-CCM+. 2023, URL https://community.sw.siemens.com/s/question/0D54O000088tuVbSAI/simulating-mooring-lines-or-cables-with-dem-fiber-in-simcenter-starccm.

[57] Hall M, Goupee A. Validation of a lumped-mass mooring line model with DeepCwind semisubmersible model test data. Ocean Eng 2015;104:590–603. http://dx.doi.org/10.1016/j.oceaneng.2015.05.035.

[58] Shih T-H, Liou WW, Shabbir A, Yang Z, Zhu J. A new k-epsilon eddy viscosity model for high Reynolds number turbulent flows: Model development and validation. Tech. rep., 1994, URL https://ntrs.nasa.gov/citations/19950005029.

[59] Wilcox DC, et al. Turbulence modeling for CFD, vol. 2, CA: DCW industries La Canada; 1998.

[60] Hirt CW, Nichols BD. Volume of fluid (VOF) method for the dynamics of free boundaries. J Comput Phys 1981;39(1):201–25. http://dx.doi.org/10.1016/0021-9991(81)90145-5.

[61] Muzaferija S. A two-fluid Navier-Stokes solver to simulate water entry. In: Proceedings of 22nd symposium on naval architecture. National Academy Press; 1999, p. 638–51.

[62] Muzaferija S. Computation of free surface flows using interface-tracking and interface-capturing methods. Nonlinear Water-Wave Interact Comput Mech, Southampton 1998.

[63] Larsen BE, Fuhrman DR. On the over-production of turbulence beneath surface waves in Reynolds-averaged Navier–Stokes models. J Fluid Mech 2018;853:419–60. http://dx.doi.org/10.1017/jfm.2018.577.

[64] Casalone P, Dell'Edera O, Fontana M, Mattiazzo G, Battisti B. Solutions to wave damping over time in CFD RANS simulations due to exponential generation of numerical turbulence. In: International conference on offshore mechanics and arctic engineering, vol. 85932. American Society of Mechanical Engineers; 2022, V008T09A084. http://dx.doi.org/10.1115/OMAE2022-81447.

[65] Davidson J, Ringwood JV. Mathematical modelling of mooring systems for wave energy converters - a review. Energies 2017;10. http://dx.doi.org/10.3390/en10050666.

[66] Vissio G, Passione B, Hall M, Raffero M. Expanding ISWEC modelling with a lumped-mass mooring line model. In: Proceedings of the 11th European wave and tidal energy conference. 2015, p. 1–9, URL https://matt-hall.ca/docs/vissio_2015_eim.pdf.

[67] Hall M. Moordyn v2: New capabilities in mooring system components and load cases. In: Proceedings of the international conference on offshore mechanics and arctic engineering - OMAE, vol. 9. 2020, http://dx.doi.org/10.1115/OMAE2020-19341, Export Date: 22 March 2024; Cited By: 8.

[68] Hall M, Sirnivas S, Yu Y-H. Implementation and verification of cable bending stiffness in MoorDyn. In: International conference on offshore mechanics and arctic engineering, vol. 84768. American Society of Mechanical Engineers; 2021, V001T01A011. http://dx.doi.org/10.1115/IOWTC2021-3565.

[69] Paduano B, Pasta E, Carapellese F, Papini G, Baltazar J, Faedo N, et al. Control co-design mooring optimisation for wave energy systems: a three-tethered point absorber case. In: IFAC world congress. 2023, http://dx.doi.org/10.1016/j.ifacol.2023.10.537.

[70] Papini G, Paduano B, Pasta E, Carapellese F, Mattiazzo G, Faedo N. On the influence of mooring systems in optimal predictive control for wave energy converters. Renew Energy 2023;218:119242. http://dx.doi.org/10.1016/j.renene.2023.119242.

[71] Pozzi N, Bracco G, Passione B, Sirigu SA, Mattiazzo G. PeWEC: Experimental validation of wave to PTO numerical model. Ocean Eng 2018;167:114–29. http://dx.doi.org/10.1016/J.OCEANENG.2018.08.028.

[72] Vissio G, Valério D, Bracco G, Beirão P, Pozzi N, Mattiazzo G. ISWEC linear quadratic regulator oscillating control. Renew Energy 2017;103:372–82. http://dx.doi.org/10.1016/j.renene.2016.11.046.

[73] Sirigu SA, Fontana M, Paduano B. Experimental identification of synthetic ropes stiffness for scaled mooring systems. In: The international conference of IFToMM ITALY. Springer; 2022, p. 891–9. http://dx.doi.org/10.1007/978-3-031-10776-4_102.

[74] Fenu B, Niosi F, Paduano B, Sirigu SA. Experimental investigation of 1:25 scaled model of pendulum wave energy converter. In: 2022 international conference on electrical, computer, communications and mechatronics engineering. 2022, p. 1–6. http://dx.doi.org/10.1109/ICECCME55909.2022.9987910.

[75] Niosi F, Begovic E, Bertorello C, Rinauro B, Sannino G, Bonfanti M, et al. Experimental validation of orcaflex-based numerical models for the PEWEC device. Ocean Eng 2023;281:114963. http://dx.doi.org/10.1016/j.oceaneng.2023.114963.

[76] Umar A, Datta TK. Nonlinear response of a moored buoy. Ocean Eng 2003;30:1625–46. http://dx.doi.org/10.1016/S0029-8018(02)00144-0.

[77] Barltrop N. Floating structures: A guide for design and analysis. Oilfield Pubns Inc.; 1998.

[78] Ohmori T. Finite-volume simulation of flows about a ship in maneuvering motion. J Mar Sci Technol 1998;3:82–93. http://dx.doi.org/10.1007/BF02492563.

[79] Shabana AA. Computational dynamics. John Wiley & Sons; 2009.

[80] Slotnick JP, Khodadoust A, Alonso J, Darmofal D, Gropp W, Lurie E, et al. CFD vision 2030 study: a path to revolutionary computational aerosciences. Tech. rep., 2014, URL https://ntrs.nasa.gov/citations/20140003093.

[81] Perić R, Abdel-Maksoud M. Analytical prediction of reflection coefficients for wave absorbing layers in flow simulations of regular free-surface waves. Ocean Eng 2017;147:132–47. http://dx.doi.org/10.1016/j.oceaneng.2017.10.009.

[82] Fenton JD. A fifth-order Stokes theory for steady waves. J Waterw Port Coast Ocean Eng 1985;111:216–34. http://dx.doi.org/10.1061/(ASCE)0733-950X(1985)111:2(216).

[83] Windt C, Davidson J, Ransley EJ, Greaves D, Jakobsen M, Kramer M, et al. Validation of a CFD-based numerical wave tank model for the power production assessment of the wavestar ocean wave energy converter. Renew Energy 2020;146:2499–516. http://dx.doi.org/10.1016/j.renene.2019.08.059.